Dione's spectral and geological properties

Katrin Stephan [a,*], Ralf Jaumann [a,b], Roland Wagner [a], Roger N. Clark [c], Dale P. Cruikshank [d], Charles A. Hibbitts [e], Thomas Roatsch [a], Harald Hoffmann [a], Robert H. Brown [f], G. Filiacchione [g], Bonnie J. Buratti [h], Gary B. Hansen [i], Tom B. McCord [j], Phil D. Nicholson [k], Kevin H. Baines [h]

[a] DLR, Institute of Planetary Research, Rutherfordstrasse 2, 12489 Berlin, Germany
[b] Freie Universität, FR Planetologie und Fernerkundung, Malteserstr. 74-100, 12249 Berlin, Germany
[c] US Geological Survey, Denver Federal Center, Denver CO 80225, USA
[d] NASA Ames Research Center, MS 245-3 Moffett Field, CA 94035-1000, USA
[e] JHU Applied Physics Laboratory, Laurel, MD, USA
[f] Lunar and Planetary Laboratory, University of Arizona, Tucson, AZ 85721, USA
[g] INAF-IASF, via del Fosso del Cavaliere 100, Rome, Italy
[h] Jet Propulsion Laboratory, California Institute of Technology, Pasadena, CA 91109, USA
[i] University of Washington, Seattle, USA
[j] Space Science Institute, Winthrop, WA, USA
[k] Cornell University, Astronomy Department, Ithaca, NY, USA

ARTICLE INFO

ABSTRACT

We present a detailed analysis of the variations in spectral properties across the surface of Saturn's satellite Dione using Cassini/VIMS data and their relationships to geological and/or morphological characteristics as seen in the Cassini/ISS images. This analysis focuses on a local region on Dione's anti-saturnian hemisphere that was observed by VIMS with high spatial resolution during orbit 16 in October 2005. The results are incorporated into a global context provided by VIMS data acquired within Cassini's first 50 orbits. Our results show that Dione's surface is dominated by at least one global process. Bombardment by magnetospheric particles is consistent with the concentration of dark material and enhanced CO_2 absorption on the trailing hemisphere of Dione independent of the geology. Local regions within this terrain indicate a special kind of resurfacing that probably is related to large-scale impact process. In contrast, the enhanced ice signature on the leading side is associated with the extended ejecta of the fresh impact crater Creusa (~49°N/76°W). Although no geologically active regions could be identified, Dione's tectonized regions observed with high spatial resolution partly show some clean H_2O ice implying that tectonic processes could have continued into more recent times.

1. Introduction

Dione, one of Saturn's major satellites, discovered by Giovanni Cassini in March 1684, exhibits several peculiar properties typical of the often geologically complex icy satellites around Saturn. Dione orbits Saturn between Tethys and Rhea at a distance of 377,396 km (6.3 R_s) and lies completely within the planet's magnetosphere (Burch et al., 2007). Therefore, interaction with energetic particles is expected to be one of the major processes influencing the surface properties of this satellite.

Further, Dione possibly interacts with, or is at least influenced by, Enceladus' activity that is responsible for the formation of Saturn's E Ring because Dione orbits in the outer parts of the E Ring, which reaches from the orbit of Mimas outward approximately to the orbit of Rhea (Hillier et al., 2007). E Ring material, micro-scopic particles consisting mostly of water ice with minor constituents of silicates, carbon dioxide and ammonia (Hillier et al., 2007), was determined to have its major source in cryovolcanic plumes (Spahn et al., 2006; Porco et al., 2006) emanating from the "tiger stripes" of the south polar region of Enceladus.

Dione is large and dense enough to have experienced geologic activity for a prolonged period of time. The mean radius is 562.53 km (Thomas et al., 2007b), which makes Dione one of the larger saturnian satellites (next-largest after Titan, Rhea and Iapetus). Dione is composed primarily of water ice, but as the third-densest of Saturn's moons (~1470 ± 12 kg m^{-3}) Jacobson et al., 2005; http://ssd.jpl.nasa.gov) after Enceladus and Titan, it must also have a considerable fraction (~45%) of rocky material (Hussmann et al., 2006).

In fact, an outward plasma flow could be associated with Dione according to data from the CDA instrument aboard the Cassini spacecraft (Burch et al., 2007). This indicates recent geologic activity causing streams of particles to be flung into space, thus revealing

the satellite to be an important source of plasma in Saturn's magnetosphere. So far, however, no geologically active region has been recognized on Dione's surface. VIMS observations point only to a possible methane–ice exosphere that appears enhanced over the polar regions which could be an indicator for material released from Dione that contributes to the E Ring (Clark et al., 2008a).

Dione was first imaged by the Voyager cameras (Smith et al., 1981, 1982), revealing a complex geological history thought to be possibly comparable with Enceladus in intensity (Plescia, 1983). Voyager images showed mostly a geologically old, densely cratered surface dating back to the early history of this satellite, similar to its neighbor Rhea. But in addition, and especially on the trailing hemisphere, Dione possesses geologically younger resurfaced regions consisting of a network of bright, linear or curved lineaments that were first believed to have been created by volcanic eruptions that deposited liquid and/or pyroclastic material along fissures and fractures (Smith et al., 1981, 1982; Plescia, 1983).

Since being placed in orbit around Saturn in July 2004, the Cassini spacecraft provided new observations of Dione. Based on data of the Cassini Imaging Science Subsystem (ISS) (Porco et al., 2004), the main geological units mapped on Voyager images were confirmed and refined (Wagner et al., 2005). However, no unequivocal evidence of volcanism has been found so far. In contrast, the geologically younger regions seem to be the result of tectonism, preferentially of extensional style like on the neighboring satellite Tethys, resulting in *horst-and-graben* structures (Wagner et al., 2007).

It was known from Earth-based telescopic spectral observations that Dione's surface is dominated by water ice, although ice absorptions in the near-infrared spectral region are not as deep as on Tethys and Rhea (Fink et al., 1976; Clark et al., 1984, 1986). A significant amount of non-ice contaminants on Dione's surface has been confirmed by new measurements of Cassini's Visual and Infrared Imaging Spectrometer (VIMS) (Brown et al., 2004; Clark et al., 2008a). Despite the fact that the exact composition of the dark material is not yet clear, hemispherical differences regarding the distribution of this material point to a probably exogenic origin with material impacting the satellite preferentially on the trailing side (Clark et al., 2008a).

Minor compounds, i.e. volatiles such as CO_2 identified in VIMS spectra of Dione (Clark et al., 2008a) were found to be common on Saturn's larger satellites like Iapetus (Buratti et al., 2005; Cruikshank et al., 2008) Hyperion (Cruikshank et al., 2007) and Phoebe (Clark et al., 2005).

Beginning in July 2004, the Cassini spacecraft performed several flybys at Dione that offered a global view of its spectral characteristics, i.e. its chemical and physical surface properties. During one targeted flyby (orbit 16) in October 2005, Cassini approached Dione at a minimum distance of 500 km. As the first imaging spectrometer operating in the saturnian system, the Cassini VIMS instrument was able to acquire spectral data of the anti-saturnian hemisphere with pixel ground resolutions as small as 2 km/pixel. The best resolved data (2–7.5 km/pixel) cover the surface from 20°N to 25°S and from 210 to 250°W (Fig. 1) which have allowed Dione's local spectral properties to be analyzed in great detail. Although VIMS observations of the remaining flybys have only relatively low pixel ground resolution (Table 2), VIMS has almost completely mapped Dione's surface during Cassini's first 50 orbits, providing an excellent global context for the high-resolution VIMS data of orbit 16.

Additionally, the Imaging Science Subsystem (ISS) (Porco et al., 2004) observed Dione simultaneously with VIMS with pixel ground resolutions up to 15 m/pixel during its closest flyby to date in orbit 16. The combination of both datasets allows the correlation of physical and compositional properties derived from VIMS measurements directly with the geological and morphological surface characteristics, including surface ages as well as photometric aspects, derived from ISS images.

In this paper we present a detailed classification of Dione's surface properties based on spectral highly resolved Cassini VIMS data and discuss their relationship to geological and morphological features that were mapped based on spatial highly resolved Cassini ISS images. The analysis in this work (a) focuses on the local region of Padua Chasmata observed at high resolution during orbit 16 and (b) interprets the results in a global context. The major scientific questions addressed in this study are: (1) Do the spectral variations correlate with geological units and, if so, are there any relations between spectral variations and surface age (indicating space weathering, e.g. increasing amount of impurities with increasing surface age)? (2) How does the local distribution of surface compounds relate to their global distribution? (3) How does the distribution of minor compounds vary across Dione's surface (locally, globally)? (4) Is the transition from dark to bright material related to any morphological and geological differences? (5) Is there any evidence for present-day geological activity?

We start with an overview of the available VIMS data set (Sections 2 and 3) followed by a detailed description of the geological mapping (Section 4) based on the Cassini ISS image base map (Roatsch et al., 2008). The spectral classification of the VIMS data (Section 5) includes: (1) a summary of requirements that have to be achieved by the classification method used; (2) a description of the chosen classification algorithm; (3) the selection process and the spectral characteristics of spectral endmembers as well as (4) an overview of the derived spectral classes. This part will be followed by a detailed discussion of the spatial distribution of these spectral classes and any possible relationship to geological surface characteristics in the Padua Chasmata region (Section 6). The final part contains the discussion of the achieved results in a global context (Section 7), i.e. testing if the spectral classes defined for the Padua Chasmata region are sufficient to describe the spectral variations of the entire surface.

In order to distinguish between spectral and geological surface characteristics, in the following sections the term "*class*" is only used for spectrally defined areas and the term "*unit*" refers only to geologically defined regions.

2. Description of available observations (VIMS)

VIMS consists of two channels – a visual (V) and a nearinfrared (NIR) - that together acquire coordinated image cubes in which each pixel represents a spectrum consisting of 352 contiguous spectral channels (Brown et al., 2004). The VIMS V instrument possesses 96 spectral channels that measure radiation between 0.35 and 1.05 μm, while the VIMS IR instrument operates between 0.86 and 5.2 μm and collects reflected light in 256 spectral channels. The spectral resolution of VIMS V and VIMS NIR is 8 and 16 nm, respectively, which is sufficient to analyze absorptions (their wavelength position, shape and band depth) of H_2O–ice at 1.04, 1.25, 1.5 and 2 μm as well as narrower and weaker absorptions like the absorption near 4.26 μm of CO_2 incorporated in the surface material. The dynamic range of 12 bit ($2^{12} = 4096$ values) makes it possible to measure relatively small variations in the band depth of the specific absorptions.

The small VIMS instantaneous field of view (IFOV) of 0.5 mrad in the nominal operation mode together with close flybys (e.g. less than 1000 km distance between the spacecraft and the satellites surfaces) provides sub-km spatial resolution sufficient for detailed spatial analyses of the spectral characteristics of the surface.

VIMS observations acquired during the sequence DIONE205 in orbit DI 016 exhibit the highest ground resolutions achieved so far (Table 1). They cover Dione's anti-saturnian hemisphere from
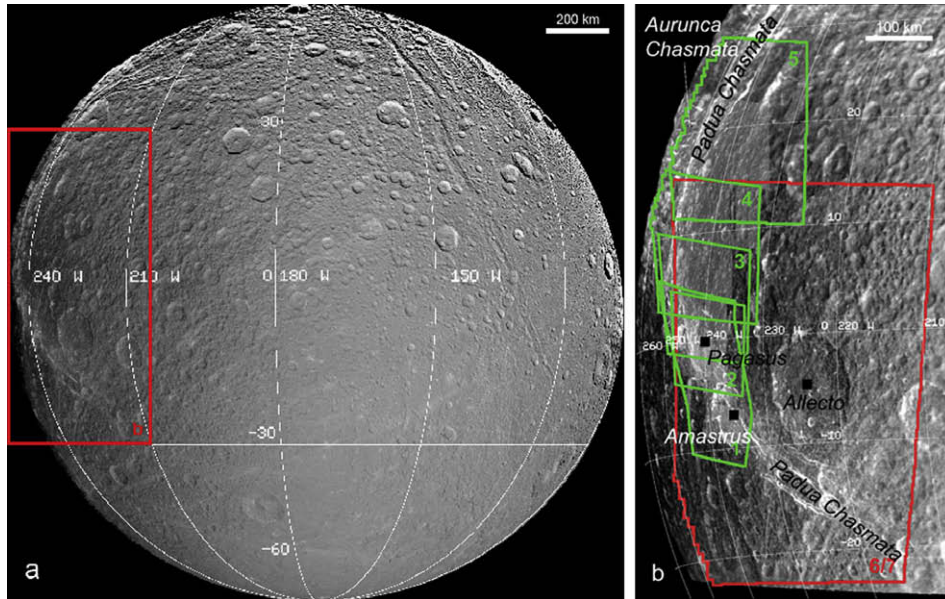
Fig. 1. Location of the study region on the anti-saturnian hemisphere (a) defined by the spatially highly resolved VIMS observation of the sequence DIONE205 acquired in orbit 16 and (b) overlaid on Cassini ISS images. All VIMS observations are listed in Table 1.

27.8°N to 26.5°S and from 210°W to 260°W with the best resolved data around 0° and 240°W (Fig. 1). Phase angles of the specific observations range between 15° and 22°. The observations partly overlap each other providing the opportunity to test the reproducibility of the mapping results and to increase the robustness of the analysis (Fig. 1). The regional and global context is provided by the remaining VIMS observations of the sequence DIONE205 of orbit 016, as well as the VIMS observations acquired during orbits 00B, 009, 026, 027, 043 and 050 (Table 2).

3. VIMS data pre-processing

VIMS data were radiometrically calibrated, i.e. the raw data number (*DN*) signal of each VIMS pixel is converted into physical values of reflectance (*I/F*). The radiance I_λ measured in [W/m^2/μm/Sr] is converted using the instrument's latest spectro-radiometric response function R_λ denoted as "RC17" in photons per *DN* (Brown et al., 2004):

$$I_\lambda = DN\tau^{-1}R_\lambda hc\lambda^{-1}(A\Omega\delta\lambda)^{-1} \qquad (1)$$

Table 1
Parameters of the Dione observations acquired during the DIONE205 sequence of orbit 16 in October 2005 exhibiting the highest pixel ground resolution that were studied in detail.

	VIMS observations	Cube size/mode	Phase angle	Geographic location	Average pixel ground resolution (km/pixel)
1	CM_1507745322_1.cub	42 × 36	15.4–17.5	3.5°N–14.5°S/233–252°W	2.83
2	CM_1507745221_1.cub	36 × 24	17.5–18.1	2.1°N–8.1°S/234–249°W	3.86
3	CM_1507745050_1.cub	36 × 24	18.3–18.9	7.7°N–5.4°S/233–256°W	4.85
4	CM_1507744874_1.cub	36 × 24	18.8–19.3	14.2°N–1.4°S/233–260°W	5.91
5	CM_1507744546_1.cub	36 × 24	19.3–19.9	27.8°N–7.8°N/231.5°–257°W	7.48
6	CM_1507744146_1.cub	48 × 42	20.5–21.4	9.8°N–23.9°S/213–250.6°W	6.33
7	CM_1507743872_1.cub	48 × 42	20.8–21.7	13.2°N–26.5°S/210–259.6°W	7.14

Table 2
Parameters of the Dione observation sequences between July 2004 and September 2007.

Cassini orbit	Observation time	VIMS observations sequences	Number of cubes	Geographic location	Average pixel ground resolution of the input cubes (km/pixel)
00B	December 2004	REGMAP001	3	47°N–52°S/276–350°W	25–17.4
		GLOCOL001	2	60°N–55°S/140–280°W	~38
009	June 2005	DIONE001	13	35°N–70°S/164–275°W	79.3–40.8
016	October 2005	DIONE205	32	60°N–85°S/96–260°W	44.5–2.9
026	July 2006	GLOCOL001	4	60°N–60°S/245–340°W	63.8–64.8
027	August 2006	REGEODB001	30	67°N–37°S/240°–320°W	66.5–97.4
		REGEODC001	24	60°N–17°S/220°–330°W	102–150
043	April 2007	REGMAPB001	5	40°N–90°S/100–360°W	29.5–60.6
050	September 2007	DIONE001	4	60°N–75°S/350–250°W	27.2–23.3
		DIONE002	6	70°N–60°S/276–67°W	13.3–29.1
		REGMAPE001	17	60°N–75°S/250–320°W	16.2–32.6
		REGMAPF001	31	76°N–70°S/270–50°W	10.0–21.5
		REGMAPG001	13	67°N–70°S/85–310°W	24.3–87.4

where τ is the exposure time in seconds, h is Planck's constant, c is the speed of light, λ is the wavelength of the particular VIMS band pass, $\delta\lambda$ is the size of the corresponding wavelength bin, A is the unobscured area of the VIMS mirror, and Ω is the solid angle subtended by a pixel in steradians. The reflectance is finally obtained by dividing I_λ by a solar spectrum (Thekekara, 1973) with the solar flux scaled for the increased Sun-target distance, R_{Z-t}:

$$I/F = I_\lambda / F_{1,\lambda} (R_{Z-\oplus}/R_{Z-t})^2 \qquad (2)$$

where $F_{1,\lambda}$ is the specific solar flux at 1 astronomical unit $R_{Z-\oplus}$. Additionally we applied a slightly revised wavelength calibration in the region of the CO_2 band at 4.25 µm following a reanalysis of the pre-launch wavelength calibration of the instrument (Cruikshank et al., 2009).

In order to combine the VIMS data set with Cassini ISS images and attribute each VIMS pixel to its geographic position, each single VIMS observation was geometrically re-projected and converted into a map-projected VIMS cube according to Jaumann et al. (2006). A nearest-neighbor algorithm was used to resample the original data during the map-projection process. This algorithm does not modify the original spectral information; it only transfers the VIMS pixel into its position in the map-projected cube. Usually, map-projections of planetary data are based on reference bodies, which describe the shape of the planetary objects. In the case of Dione a tri-axial ellipsoid is defined as a reference in the report of the International Astronomical Union (Seidelmann et al., 2002) and parameters to calculate the surface intersection point of each pixel were taken from Roatsch et al. (2008).
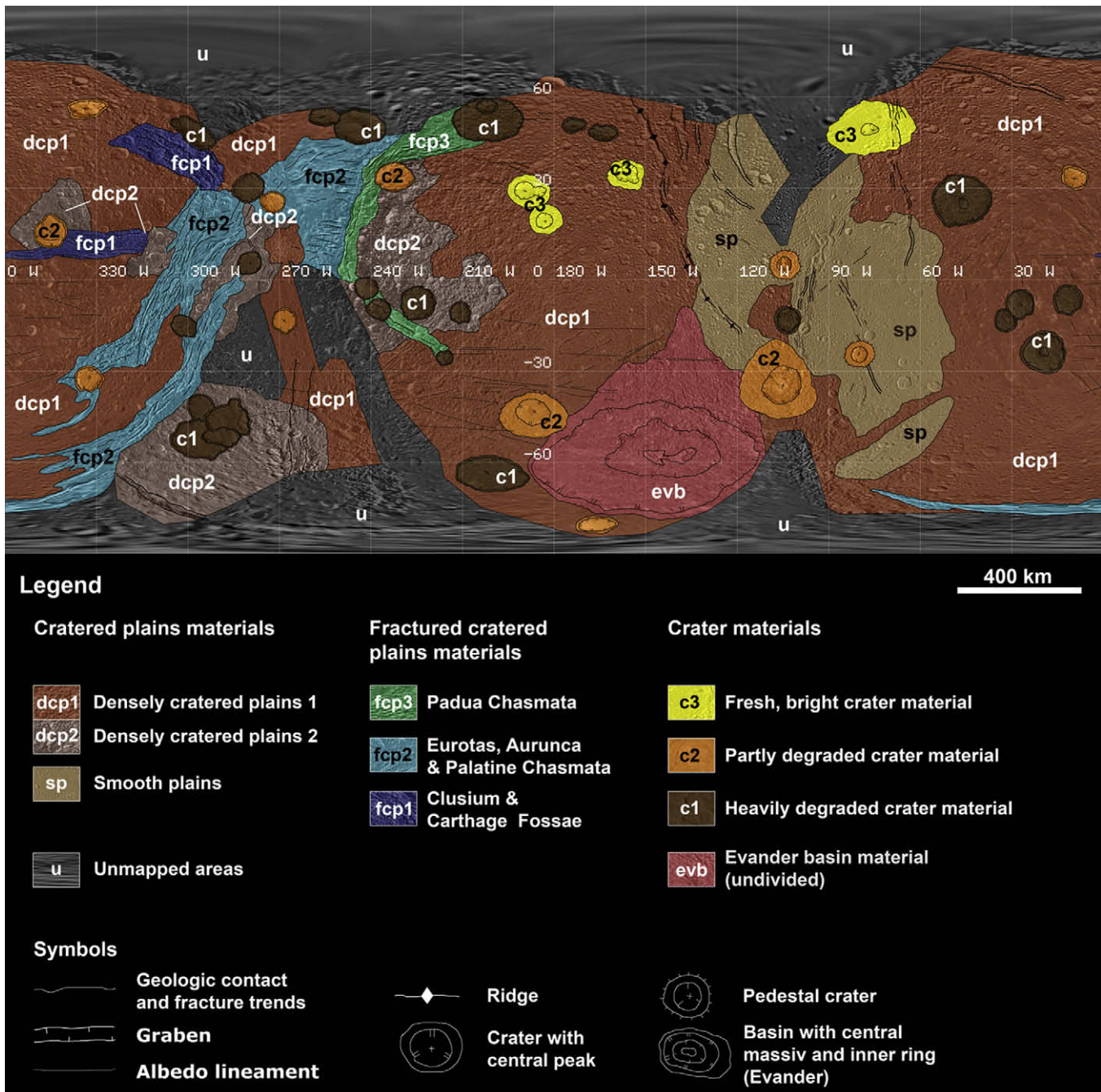

Fig. 2. Distribution of Dione's major geological units defined by albedo, morphological characteristics and impact crater frequency distributions seen in the Cassini ISS base map by Roatsch et al. (2008), shown in equidistant projection centered at 0°N and 180°W.

The final step of the VIMS data preparation is the combination of the VIMS observation into a regional mosaic of the Padua Chasmata region (Fig. 1) and a global VIMS Dione mosaic that fits to the global geological map of Fig. 2. In order to prevent deleterious effects arising from the projection of low signal-to-noise data, the mosaicking was done after the spectral analysis of the data set and only combines the results of each single VIMS observation into the final mosaics.

4. Geological mapping

In order to relate spectral to geological and morphological surface properties, we mapped the distribution of Dione's major geological units using the Cassini ISS base map published by Roatsch et al. (2008) at a reduced map scale (1 km/pixel), which is sufficient for comparison with the lower resolution VIMS data (Fig. 2). For mapping geologic details, individual Cassini ISS images (CLEAR filter) were used at their original image resolution. Geological units were identified by (a) albedo, (b) morphological characteristics, and (c) impact crater frequency distributions. The geologic units described here are considered to be three-dimensional material units rather than "terrain types" – regardless of their spatial extent and morphology (Wilhelms, 1990). Pre-Cassini studies, based on Voyager imagery by Plescia (1983) und Moore (1984) as well as preliminary results obtained with Cassini ISS images by Wagner et al. (2005, 2006) were used as a reference. Mapping of geologic units and the correlation between global and regional maps was challenged using ISS and Voyager imaging data taken under very different illumination conditions, viewing angles and spatial resolutions. Additionally, there are areas on Dione not yet very well imaged by Cassini ISS, especially the northern latitudes. Areas where no exact identification of geologic units was possible were classified as *unmapped areas* (*u*) (dark gray color in Fig. 2).

In general, geologic units on Dione can be combined into four major groups: (1) *densely cratered plains* (*dcp*), (2) *smooth plains* (*sp*), (3) *fractured cratered plains* (*fcp*), and (4) *impact crater materials*.

4.1. Densely cratered plains (dcp)

The densely cratered plains (*dcp*) are the most abundant unit on Dione (Wagner et al., 2005, 2006) and were also identified in Voyager images where they were as *heavily cratered terrain* (Plescia, 1983). They are characterized by high albedo and rough morphology caused by rims of densely packed impact craters at all sizes and degradation states. Crater counts in various areas of *dcp* across Dione revealed a production distribution close to equilibrium, and cratering model ages on the order of 4 byr (Plescia and Boyce, 1985; Zahnle et al., 2003; Neukum, 1985; Neukum et al., 2006) making this the oldest geological unit on Dione. By examining Cassini ISS images at their original resolution, unit *dcp* could be divided into two different facies (*dcp*1 and *dcp*2) despite the very oblique viewing geometry during this flyby (Fig. 3). Unit *dcp*1 represents relatively unaltered densely cratered plains and the second facies, *dcp*2, shows several large impact craters intersected by a smooth or hummocky, gently rolling, less densely cratered surface. The facies *dcp*2 was not identified in Voyager images. This facies has an irregular boundary (no preferred orientation) with *dcp*1. Although crater size-frequency measurements are difficult because of the oblique viewing angle making the exact measurement of crater diameters rather difficult, *dcp*2 is depleted in small impact craters (diameter < 30 km) (Fig. 2), which is indicative of resurfacing (see discussion in Section 6).
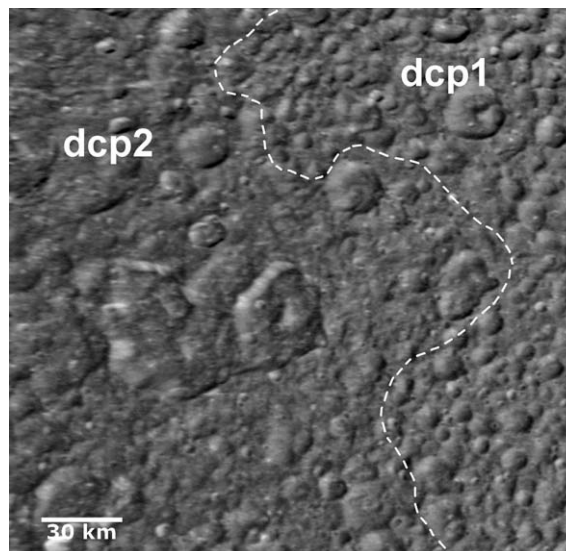

Fig. 3. Close-up view of the boundary between the two facies (indicated as *dcp*1 and *dcp*2) of the densely cratered plains in the ISS-NAC image N1596421410 centered at 60°N and 130°W.

4.2. Smooth plains (sp)

Smooth plains on Dione primarily differ from the densely cratered plains by their lower crater frequencies (Fig. 2). This unit correlates with plains units (comprising, e.g., *cratered plains* and *lightly cratered plains*) identified by Plescia (1983) in Voyager data. We remapped the geologic boundary between *sp* and *dcp*1, making use of the higher resolution of Cassini ISS data which, in addition, extended into the area not imaged by Voyager. An ovoid-shaped area of this unit is located at high southern latitudes. This unit locale is consistent with *lobate deposits* mapped by Plescia (1983). Low-resolution images from several orbits obtained under relatively low Sun revealed scarps at its outer boundary, indicating that this ovoid-shaped area is higher than the surrounding terrain.

4.3. Fractured cratered plains (fcp)

Despite the high crater frequency and the mostly old age of the surface, Dione has a large number of tectonic features indicating a past period of intense endogenic activity (Fig. 2). Preferentially on the trailing hemisphere, bright wispy markings were observed and mapped (Smith et al., 1981). These bright lineaments, which were originally termed "wispy streaks", "wispy markings", or *lineae* on USGS topographic maps derived from the Voyager flybys, were interpreted as pyroclastic deposits resulting from eruptions along cracks in Dione's surface along linear to curved fractures during Dione's early geologic history (e.g., Smith et al., 1981, 1982). It was also anticipated that tectonism could have played a major role in shaping the trailing hemisphere which hosts most of the bright *lineae* (Moore, 1984). Indeed, Cassini images have revealed that the lineaments represent sets of parallel deep, wide graben, scarps, or troughs, in parts with interstitial horsts, indicative of extensional and shear stresses (Wagner et al., 2006). Ridges that may imply compressional stresses also occur on Dione but not in the local region observed by VIMS at high spatial resolution. Recently, the features previously termed *lineae* were renamed to either *chasmata* or *fossae* to account for their specific morphologies (Roatsch et al., 2008).

The unit *fcp* represents the youngest geological units in this work. Although fewer in number, impact craters are still to be seen within this unit, and they exhibit different degrees of degradation

but retain bright rims. According to crater size-frequency measurements carried out in a part of the fractured cratered plains at regional spatial resolution (Wagner et al., 2006), the tectonic episodes could date back to 3.7 byr (with uncertainties on the order of 100 myr) given a lunar-like flux model of Neukum et al. (2006) or to 1 byr using the constant flux model of Zahnle et al. (2003). Note, that for the latter model, however, the range of ages is 2.7 byr to 260 myr due to uncertainties of the cratering rates.

The unit *fcp* could be subdivided into three facies of different ages. Two systems of troughs, named *Carthage* and *Clusium Fossae*, are truncated by the S-shaped bands of *Eurotas* and *Aurunca Chasmata* and are therefore stratigraphically older. They are mapped here as *fractured cratered plains* 1 (*fcp*1). *Eurotas* and *Aurunca Chasmata*, which dominate the center of Dione's trailing hemisphere as well as the southern bands of the *Palatine Chasmata*, are defined here as *fractured cratered plains* 2 (*fcp*2). The *fractured cratered plains* of Padua Chasmata crosscut *Eurotas*, *Aurunca* and *Palatine Chasmata* (unit *fcp*2), and therefore youngest of these tectonic units, defined as unit *fcp*3. These sets of graben and scarps form a semicircle and border units *dcp*2 and also *dcp*1. Other tectonic structures that are not characterized by strong albedo differences compared to the cratered plains units are indicated by symbols on the map.

4.4. Impact crater material

Impact crater materials were subdivided into three erosional units (Fig. 2). Pristine, and in some cases bright crater materials are mapped as unit *c*3. Craters of this *c*3 unit are interpreted to be the youngest. Rims, central peaks, and if discernable, ejecta materials are slightly degraded in the next older crater unit *c*2. The crater unit with the highest degree of degradation and therefore the greatest age is *c*1, whose rims, etc. are mostly heavily degraded. The great age of these craters is also indicated by the high frequency of superimposed craters. The prominent 400 km large impact basin *Evander* was mapped as a single, undivided unit (*evb*). Evander is a two-ring basin with a central peak massif and a relaxed topography, as revealed in stereo images (Wagner et al., 2006).

The Padua Chasmata region observed during orbit 16 with high spatial resolution contains six of the previously described geological units on Dione (Fig. 4). The region is named after its dominating tectonic structure, the Padua Chasmata (*fcp*3), which form a semicircle centered approximately at 12°N and 212°W (with the eastern semicircle part missing). The Padua Chasmata represent the youngest tectonic unit in this area. The Aurunca Chasmata (*fcp*2), the next older graben system, are only marginally seen near the western limb in Fig. 4, where they are truncated by the graben, scarps and troughs of the Padua Chasmata system. The most extended geological unit in this region is the facies 2 of the densely cratered plains (*dcp*2) followed by facies 1 (*dcp*1) in the eastern part of our region of interest. Impact craters in the Padua Chasmata region were found to belong to units *c*1 and *c*2. The most prominent impact craters that are located in the *dcp*1 or *dcp*2, are craters Allecto (106 km) and Entellus (63 km) (the latter partly located in unit *dcp* and *fcp*). The impact craters Tereus, Pagasus and Amastrus are located within the tectonic structures of the Padua Chasmata (Figs. 1 and 4).

Additionally, bright linear features crossing units *dcp* and *fcp* in the lower right of the observed region were recognized to be a set of radial scarps originating from a point at 39.8°S and 246.2°W (Wagner et al., 2006). From Voyager images, this feature was erroneously interpreted as a ray crater and named Cassandra (Plescia, 1983). The feature name Cassandra has now been relocated to a small crater near the source region of the radial scarps (Roatsch et al., 2008). Because these linear features are very narrow relative
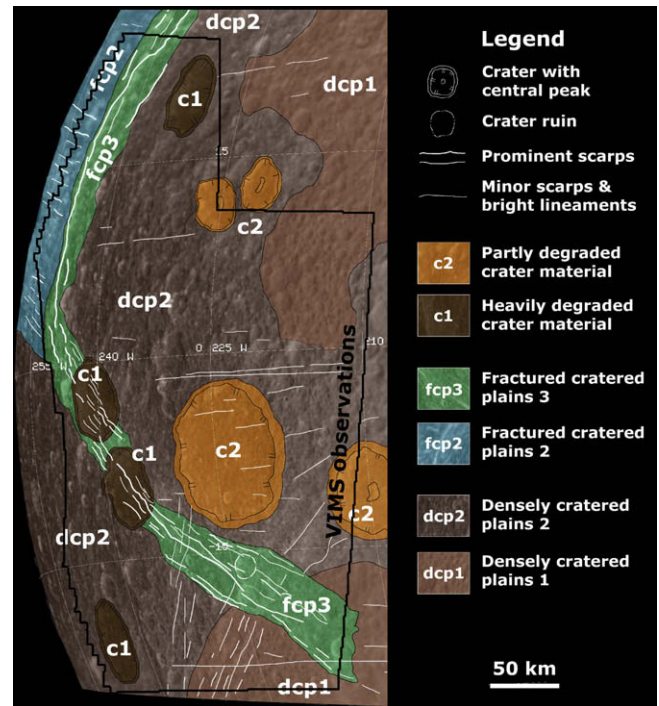

Fig. 4. Geological map of the Padua Chasmata region shown in an orthographic projection centered at 3°S and 177°W.

to the pixel ground resolution of ISS images and VIMS data they could not separately be analyzed (Fig. 4).

5. Spectral classification of the VIMS data

H_2O–ice is the most abundant surface material on Dione's surface and the spectrally dominant compound in all VIMS spectra. Secondly, rocky non-ice material exists on Dione's surface and minor amounts of volatiles such as CO_2 and organics are suspected (Clark et al., 2008a). On icy satellites like Dione, however, not only compositional but also physical aspects are significant and essential for understanding the interaction between surface properties and surface processes i.e. specific sizes of the H_2O–ice particles, their crystallinity, their style of mixing with additional non-ice compounds, thermal processing, and exogenic influences.

Some of these physical properties cannot be retrieved from single spectral characteristics like absorption band depths but from the combined analyses of all spectral characteristics that appear in a reflectance spectrum of H_2O–ice (Stephan, 2006). These compositional and physical surface characteristics usually cause specific changes in (a) overall albedo, (b) the local slope of the spectral continuum at a given wavelength, (c) the existence of absorption signatures and (d) their spectral parameters i.e. wavelength position, shape and band depth. The detailed analysis of specific compositional and physical properties usually requires extensive spectral modeling of individual measured spectra using photometric equations, such as those developed by Hapke (1981) and Shkuratov et al. (1999). Therefore it is prohibitive to perform a pixel by pixel analysis of an extended data set like the Dione VIMS data.

In addition, the VIMS data studied here contain numerous Dione observations that were acquired under diverse observation conditions, which also significantly influence the spectral characteristics. These include (a) pixel ground resolution, (b) exposure duration, which affects the signal-to-noise-ratio (SNR) and limits the ability to detect weak absorptions, as well as (c) observation

geometry and illumination conditions, which affects the absolute reflectance within a specific wavelength range.

In order to study the spectral variations across Dione's surface a classification method is required that enables (a) the rapid analysis of the extended dataset on a pixel by pixel base over the full wavelength range of VIMS taking into account all of Dione's spectral properties mentioned above, (b) the mapping of the derived spectral variations in a manner that (c) is insensitive to differences due to observation conditions.

5.1. Spectral Angle Mapper (SAM)

The Spectral Angle Mapper (*SAM*) is one of the leading and widely used classification techniques, which is considered a successful method for mapping the spectral similarity of image spectra to previously defined reference spectra (Yuhas et al., 1992; Kruse et al., 1993; Van der Meer et al., 1997; Crosta et al., 1998; De Carvalho and Meneses, 2000; Schwarz and Staenz, 2001; Hunter and Power, 2002; Girouard et al., 2004). SAM not only provides a means to analyze the complete VIMS spectrum in one step but can also repress influences caused by varying surface illumination conditions in order to accentuate the target reflectance characteristics (Kruse et al., 1993; De Carvalho and Meneses, 2000).

SAM is based on the assumption that each observed spectrum is a vector in an *n*-dimensional coordinate system, where *n* equals the number of spectral channels. Each spectrum or vector is characterized by both the magnitude (length) and angle measured with respect to the axes (Richards and Jia, 1996). Only the angular information is used for identifying pixel spectra in the *SAM* technique (Kruse et al., 1993). This makes *SAM* results invariant to unknown multiplicative scalings (i.e. multiplication of *x* and *y* by constants over the full wavelength range of VIMS), and consequently, invariant to unknown deviations that may arise from different illumination and observation geometry (Keshava and Mustard, 2002). Albedo differences caused by compositional changes, which certainly occur in the Dione spectra, only affect specific parts of the VIMS wavelengths range and therefore do not represent multiplicative scalings. Thus the *SAM* is more suitable when analyzing regions with significant illumination differences.

In order to compare two spectra, i.e. a VIMS spectrum, and the reference spectrum the multidimensional vectors are defined for each spectrum and the angle between the two vectors is calculated using the arccosine function:

$$\alpha = \cos^{-1} \left[\frac{\sum_{i=1}^{n} x_i y_i}{\left(\sum_{i=1}^{n} x_i^2 \right)^{1/2} \left(\sum_{i=1}^{n} y_i^2 \right)^{1/2}} \right] \qquad (3)$$

where *n* represents the number of spectral channels, x_i the VIMS spectra and y_i the reference spectrum (Yuhas et al., 1992; Kruse et al., 1993; Van der Meer et al., 1997; De Carvalho and Meneses, 2000). Smaller angles represent closer matches to the reference spectrum. If this angle is smaller than a given tolerance level, the spectra are considered to match. Pixels further away than the specified maximum angle threshold are not classified (Lillesand and Kieffer, 2002).

5.2. Spectral endmember selection

Reference spectra usually represent "pure" *spectral endmembers* mixed in the target material. These *spectral endmembers* should reflect Dione's spectral properties as closely as possible including also weak absorptions (like the one caused by CO_2) as well as physical characteristics like different size of H_2O particles. In order to get an overview of Dione's most important spectral characteristics that should be taken into account during the classification process, average VIMS spectra were selected for specific regions in the VIMS

data, which correspond to individual geologic units as seen in the Cassini images (Figs. 2 and 4). This was done based on the assumption that spectral variations across Dione's surface mainly occur in close correlation to surface processes that are responsible for the development of these geological units.

Because of relatively short integration times the reflectance spectra of the global VIMS observations (Table 2) are often dominated by noise especially at long wavelengths (>3 μm) that makes the spectral analysis rather difficult. Especially weak and/or narrow spectral signatures are not recognizable at all. Only the high-resolution VIMS cubes acquired during orbit 16 (Table 1) that cover the Padua Chasmata region, exhibit sufficiently high *SNR* at all wavelength (>100), which allows the detailed analysis of Dione's spectral properties and, therefore, were used for the first step of our spectral analysis.

Fig. 5a shows the average spectra selected for each of the six geological units according to the geological map of the Padua Chasmata region (Fig. 4). Since the individual VIMS spectra corresponding to a specific geologic unit come from multiple VIMS observations acquired under different viewing geometries (Table 1) all average spectra in Fig. 5 were normalized at 2.73 μm, where all spectra show a strong negative slope in the left wing of the strong H_2O–ice absorption at 3 μm, in order to avoid the influence of different phase angles onto the spectral characteristics.

Although all six spectra are dominated by H_2O–ice indicated by the strong absorptions at 1.5, 2, 3, and 4.5 μm (Fig. 5a), small but distinct differences between these spectra are apparent. At wavelengths shorter than 0.8 μm, the spectra appear quite different from those of H_2O–ice (Fig. 5a and b). Despite the fact that all spectra can be distinguished with respect to their general albedo in this wavelength range, they all show a significant peak at 0.5 μm possibly created by scattering due to particles (i.e. carbon grains) smaller than 0.5-μm in diameter embedded in the surface ice as proposed by Clark et al. (2008a,b). Further, the spectra are influenced by an UV-absorber responsible for the steep slope from 0.5 μm to shorter wavelengths, with the strength probably indicating the amount of this contaminant (Clark et al., 2008a). Table 3 summarizes relevant spectral parameter calculated for the six average spectra, which also includes the slope of the spectral continuum between 0.5 and 0.35 μm (VIS 1):

$$\text{VIS1} = \frac{I/F_{0.5\mu m} - I/F_{0.35\mu m}}{\Delta\lambda}; \quad \Delta\lambda = 0.15 \; \mu m \qquad (4)$$

The measured slopes VIS 1 do not change significantly between the six average spectra indicating that the nature of the UV-absorber (Clark et al., 2008b) remains constant across Dione's surface in the Padua Chasmata region.

Major spectral differences between the six average spectra occur in the near-infrared spectral range. The spectral variations generally range from a less ice-dominated spectrum #6 to the nearly pure H_2O–ice spectrum #1. These differences are related to variations in the overall albedo and slope of the spectral continuum especially between 0.5 and 2.3 μm, as well as to the existence or non-existence of H_2O-absorptions and absorptions of minor compounds like CO_2, as well as changes in their spectral parameters i.e. absorption band depth. The six average spectra differ from each other at least in one of these spectral characteristics.

In general, the albedo in the visible and near-infrared decreases, the slope of the spectral continuum from 0.5 μm towards 3 μm flattens and the strong H_2O-absorptions weaken continuously when moving from spectrum #1 to #6 (Fig. 5). The spectral slope (VIS 2) was measured between 0.5 μm and 2.2 μm, the latter defining the maximum reflectance between the H_2O-absorptions 2 and 3 μm:
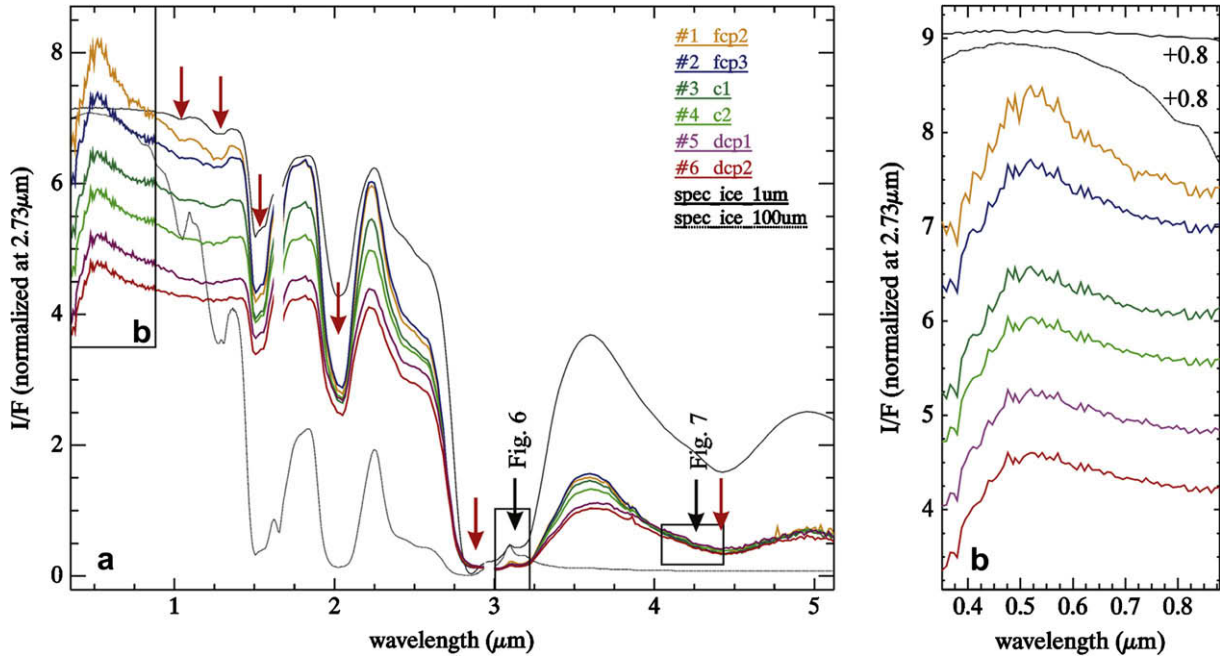
Fig. 5. Average spectra derived for six geological units in the Padua Chasmata region shown in comparison to H_2O–ice model spectra for specific grain radii (1 and 10 μm) developed by Hansen (2008) (a) for the full wavelength range of the VIMS instrument and (b) separately for the visible wavelength range.

$$VIS2 = \frac{I/F_{0.5\mu m} - I/F_{2.2\mu m}}{\Delta\lambda}; \quad \Delta\lambda = 1.8 \qquad (5)$$

The slope increases from average spectrum #6 to #1 due to the higher spectral dominance of H_2O–ice and/or larger ice grains. Spectrum #1 exhibits a clear signal of H_2O–ice including the weak absorptions at 0.9, 1.04 and 1.25 μm in addition to the deepest absorption of H_2O–ice at 1.5, 2, 3 and 4.5 μm (Fig. 6). Absorptions band depths of the six average spectra summarized in Table 3 were derived according to Clark and Roush (1982) and Clark et al. (2003). Although the deepening of the H_2O-absorptions from spectrum #6 to spectrum #1 is supported by the values in Table 3, the absorption at 1.5 μm increases more strongly from spectrum #2 to spectrum #1 (32% to 35.5%) compared to the absorption at 2 μm (60–60.5%), which could point to larger H_2O grain sizes in spectrum #1. In general, H_2O–ice absorptions deepen with increasing size of the ice particles. However, correlation curves of absorption band depths derived by Stephan, (2006) based on H_2O–ice models developed by Hansen and McCord (2004) and Hansen (2008) show that with increasing grain size the stronger H_2O-absorptions enter an area of band saturation i.e. the depth of the absorptions does not increase very strongly anymore and decreases again when the absorptions are fully saturated. This occurs for the absorption at 2 μm at relatively smaller grains than for the absorption at 1.5 μm. Thus the disproportional increase in the depth of the absorptions at

1.5 μm and 2 μm could indicate larger ice grains in spectrum #1 compared to spectrum #2.

Additionally, spectrum #1 shows a distinct reflection peak at 3.1 μm that is more complex in comparison with the peak in the remaining spectra characterized by a simple shape of this feature (Fig. 6). Usually the appearance of Fresnel reflection peak at 3.1 μm is diagnostic of the existence of crystalline or amorphous H_2O–ice (e.g. Hansen and McCord, 2004) with a more pronounced and complex structure in case of crystalline and a simpler shape in case of amorphous H_2O–ice. Recent studies also show that the peak is more pronounced in larger ice grains (Clark et al., 2009) supporting our assumption made above. Thus, crystalline ice in addition to larger ice grains could explain spectrum #1. In contrast, the remaining spectra exhibit no crystalline ice or are influenced by scattering effects caused by smaller ice grains. Further, the weak H_2O-absorptions at 1.04 and 1.25 μm are subdued in spectra #2 and #3 and not visible at all in the spectra #4 to #6 due to the increasing spectral influence of non-ice contaminants. Here the overall spectral slope from 0.8 to about 2.3 μm of the average spectra is flat and appears to be caused by a broad absorption, which extends from visible to infrared wavelengths and is centered at 1 μm (Clark et al., 2008a) (Fig. 5a). Although the composition of the dark material is still not solved, Clark et al. (2008a) state that H_2O–ice mixed with 200 nm diameter carbon grains that cause the scattering effect, and nano-phase hematite as the UV-absorber,

Table 3
Spectral parameters of the spectral classes i.e. slopes between 0.5 and 0.35 μm (VIS1) and 0.5 and 2.3 μm (VIS2) as well as depths of the H_2O–ice absorptions at 1.04, 1.25, 1.5 and 2 μm. The inaccuracies of the measured values were determined based on the SNR of the individual VIMS spectra in the specific wavelength range averaged over the specific regions selected for the six average spectra. Measured values that do not exceed the noise signal were excluded.

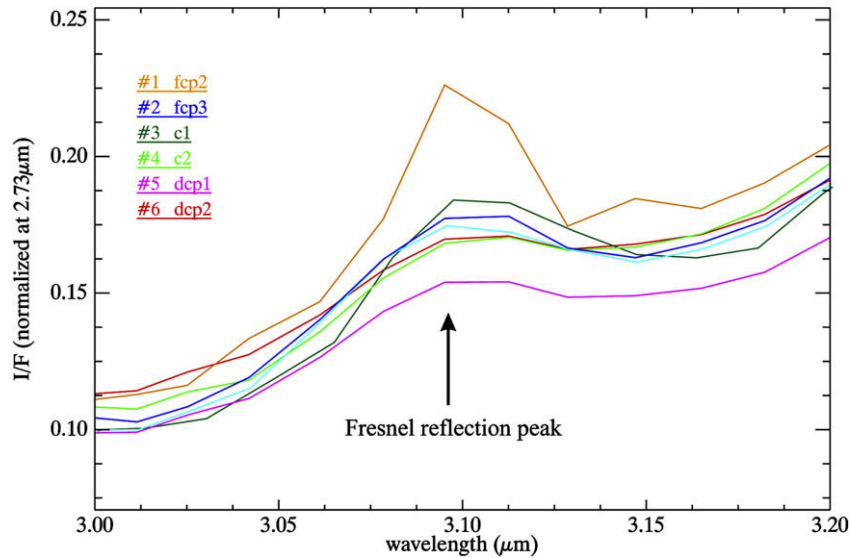| Spectral class	VIS 1	VIS 2	BD 1.04 μm	BD 1.25 μm	BD 1.5 μm	BD 2 μm	BD 4.25 μm
#1	0.64(±0.03)	0.13(±0.03)	0.03(±0.01)	0.04(±0.005)	0.355(±0.05)	0.605(±0.02)	–
#2	0.67(±0.03)	0.1(±0.03)	–	0.025(±0.006)	0.32(±0.05)	0.60(±0.02)	–
#3	0.67(±0.03)	0.09(±0.03)	–	–	0.21(±0.05)	0.50(±0.02)	–
#4	0.73(±0.03)	0.07(±0.03)	–	–	0.29(±0.05)	0.59(±0.02)	0.09(±0.05)
#5	0.67(±0.03)	0.055(±0.03)	–	–	0.20(±0.05)	0.47(±0.02)	0.11(±0.05)
#6	0.67(±0.03)	0.04(±0.03)	–	–	0.20(±0.05)	0.45(±0.02)	0.09(±0.05)

Fig. 6. Average spectra like in Fig. 5 separately for the wavelength region of the Fresnel reflection peak at 3.1 μm showing a pronounced peak in the spectrum derived from geological unit *fcp*2 in comparison of a subdued peak in the remaining average spectra (Fig. 5).

closely match the Dione spectra. This absorption feature is most prominent in spectra #5 and #6 and is accompanied by relatively shallow H_2O–ice absorptions at 1.5 and 2 μm.

In addition to the H_2O-absorptions, the average spectra of Fig. 5 partly show an absorption of gaseous CO_2 at ~4.25 μm incorporated into the surface material, which has been found surprisingly widely distributed on the saturnian satellites surfaces (Buratti et al., 2005; Clark et al., 2008a,b; Cruikshank, 2009). The absorption of CO_2 is very weak and often difficult to identify in the VIMS spectra due to a low *SNR* in this wavelength range (Fig. 5a). Covariance statistics (i.e. eigenvectors) offer the possibility to separate the noise component and possible systematic instrument artifacts from the spectra, and are therefore useful to verify the identification of weak absorptions as described in detail by Stephan et al. (2008a,b). In particular, eigenvectors calculated for the specific wavelength range from 4 to 4.5 μm, where CO_2 is assumed to be the only spectrally active compound, show that the first order eigenvector is dominated by the absorption of CO_2 at 4.25 μm (Fig. 7a). Higher-order eigenvectors become more and more dominated by instrument artifacts and noise signal.

The depth of the CO_2-absorption is uniformly very weak in the average spectra of the geological units and does not exceed 11% measured relative to the spectral continuum (Fig. 7b). Nevertheless small variations are apparent, indicating a deeper absorption in spectrum #6 as well as in spectra #5 and #4. The CO_2-absorption is even weaker and difficult to recognize, if existent at all, in the ice-dominated spectra #3, #2 and #1. Measured band depths lie completely within the inaccuracy of the VIMS signal of 5% as derived for the VIMS spectra of Dione in this wavelength region (Cruikshank, 2009). The wavelength position and/or shape of this absorption remain constant implying that the physical nature of the CO_2 does not vary within the Padua Chasmata region.

Based on the assumption that the six average spectra described above reflect the major spectral characteristics that can be mapped across Dione's surface and based on the fact that they are spectrally unique i.e. that they differ in at least one spectral characteristic, these spectra were used as *spectral endmembers* for the *SAM* classification process.

5.3. Statistics of the derived spectral classes

A maximum angle of 0.05 radians was found to be sufficient as the maximum acceptance angle between the vector of the *endmember spectra* and the vectors of the individual VIMS pixel in order to classify the VIMS data of the Padua Chasmata region completely i.e. the derived spectral classes fully cover the region of interest. Only pixels in which the signal is partly missing due
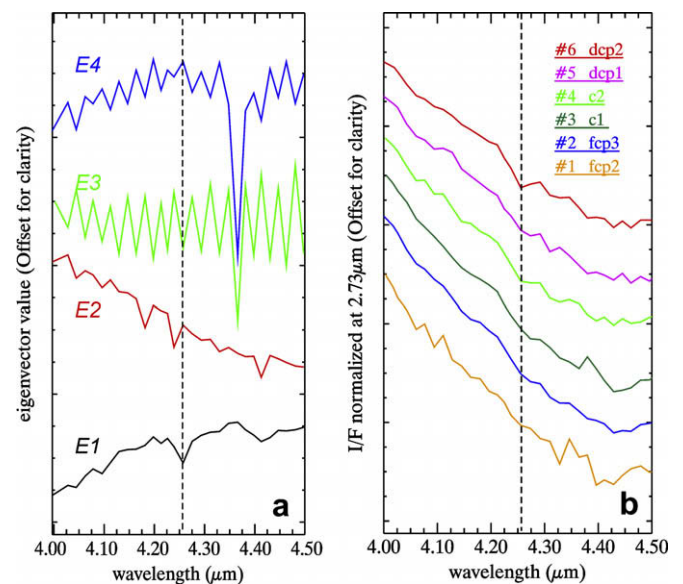

Fig. 7. The absorption of CO_2 at 4.25 μm incorporated in the surface material of Dione as identified (a) using covariance statistics (especially the eigenvectors) here illustrated for the VIMS observation CM_1507745221_1 that shows the dominance of the CO_2-absorption in the first eigenvector in contrast to the increasing noise component in the higher-order eigenvectors and (b) in the average spectra of the six spectral units of Fig. 5 shown here separately for the wavelength region between 4 and 4.5 μm. The absorption is deepest (<11% relative to the spectral continuum) in spectrum #6 (*dcp*2) and still suspected in spectra #5 and #4 and possibly in spectra #3 and #2. Only the spectrum #1 (*fcp*2) shows no absorption at all.

to instrumental effects especially in the 1–1.4 µm (Clark et al., 2008a) could not be classified but were taken into account in the analysis nevertheless by manual inspection.

Fig. 8 illustrates the statistics of the six spectral classes resulting from *SAM* classification over the full wavelength range by plotting the minimum, maximum and mean spectrum as well as ± one standard deviation for each of them. The spectral classes are numbered with respect to their corresponding *endmember spectra*. As discussed above, the SAM analysis was performed using the original *endmember spectra* i.e. without normalizing them. In order to illustrate the derived spectral classes, however, spectra in Fig. 8 were again normalized at 2.73 µm to enhance their spectral differences. The spectral classes differ accordingly to the characteristics of the six *spectral endmembers* as described above (Fig. 5; Table 3), but nevertheless illustrate the continuous variations in the spectral properties in the Padua Chasmata region. No region with completely different spectral characteristics could be identified in the data set.

Fig. 9 shows the statistics of the six spectral classes separately for the wavelength region of the CO_2-absorption at ∼4.25 µm. Min and Max spectra of each class reflects the difficulty to map the distribution of CO_2 on Dione's surface on a pixel by pixel basis due to small absorption band depth and the low *SNR* in this wavelength region. Nevertheless, the "statistical" spectra (esp. the Mean as well as the standard deviations) support the spectral characteristics indicated by the *endmember spectra*. A weak absorption of CO_2 can still be suspected in the Mean spectra of the spectral classes #5 and #6 in comparison with the corresponding *endmember spectra* but is not recognizable if present at all in the spectral classes #4 to #1.

6. Distribution of the spectral classes in and implications to the geological history of the Padua Chasmata region

Each of the six spectral classes derived by SAM will now be discussed with respect to and possibly attributed to specific chemical and/or physical surface properties, their spatial distribution in the Padua Chasmata region and possible relationships to geological units as well as implication to Dione's geological history. Finally, results will be extrapolated to retrieve significant information of global context as revealed by these spectral variations on Dione, testing in particular if the *spectral endmembers* described in Section 5 are enough to explain the spectral variation of the whole satellite.

Fig. 10 shows the SAM results separately for each of the six spectral classes overlaid onto the corresponding ISS images, from which we can address possible relationships between the specific spectral class, its spectral characteristics and spatial distribution with morphological and geological surface properties as presented in the geological map of Fig. 4.

6.1. Spectral class #1 (orange)

The *spectral class* #1 is the only class that exhibits a clean H_2O–ice signature (except the reflection peak at 0.5 µm) as introduced above including the weak H_2O-absorptions at 1.04 and 1.25 µm in addition to the strong absorptions at 1.5, 2, 3 and 4.5 µm as well as the pronounced Fresnel reflection peak at 3.1 µm that points to a crystalline ice structure.

Fig. 11 illustrates the comparison between the depths of the H_2O-absorptions at 1.04, 1.25, 1.5 and 2 µm measured in the individual VIMS spectra of spectral class #1 and as derived from H_2O–ice model spectra developed by Hansen (2008). Although a contamination with non-ice contaminant and different mixing styles of H_2O particles within each of these VIMS pixel cannot be fully excluded, the comparison implies average grain radii of less than 10 µm (Fig. 11).

So far, pure H_2O–ice detected on an icy satellite appears to be an indicator for geologically very young, possibly recently active surfaces such as the ongoing deposition of water frost (Stephan, 2006) and the cryovolcanic activity on Enceladus (Brown et al., 2006; Jaumann et al., 2008). Older surfaces of icy planetary objects in general show distinct contaminations with non-ice materials, probably 'rocky' or 'organic' impurities (Prockter et al., 1998; Stephan, 2006). Only a few percent of contaminants subdue the spectral signatures of H_2O–ice completely, especially in the shorter wavelength ranges (Dozier, 1989; Clark et al., 1984). Since previous
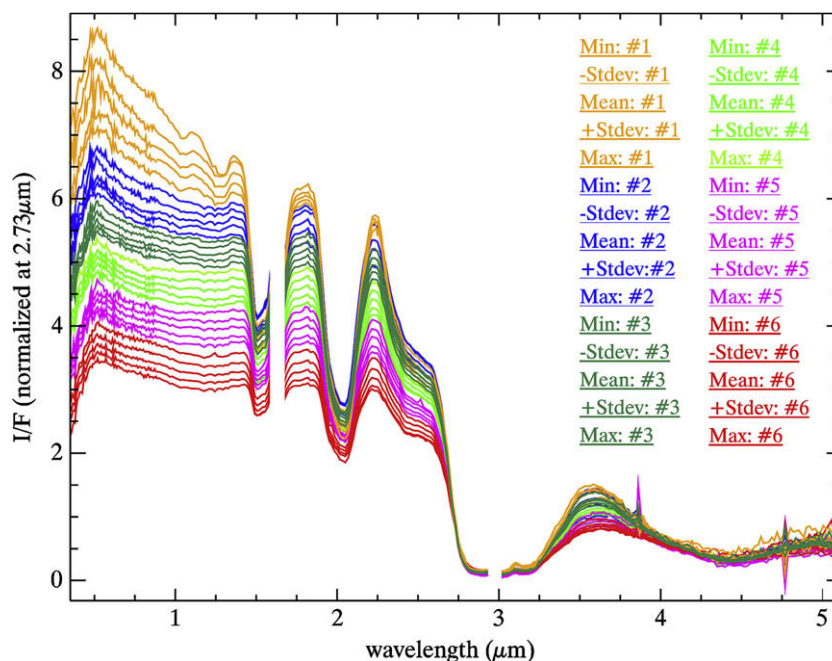

Fig. 8. Statistics (i.e. Min, −Stdev, Mean, +Stdev, Max from the bottom to the top spectrum of each class, respectively) of the spectral classes #1–#6 derived by SAM over the full VIMS wavelength range.
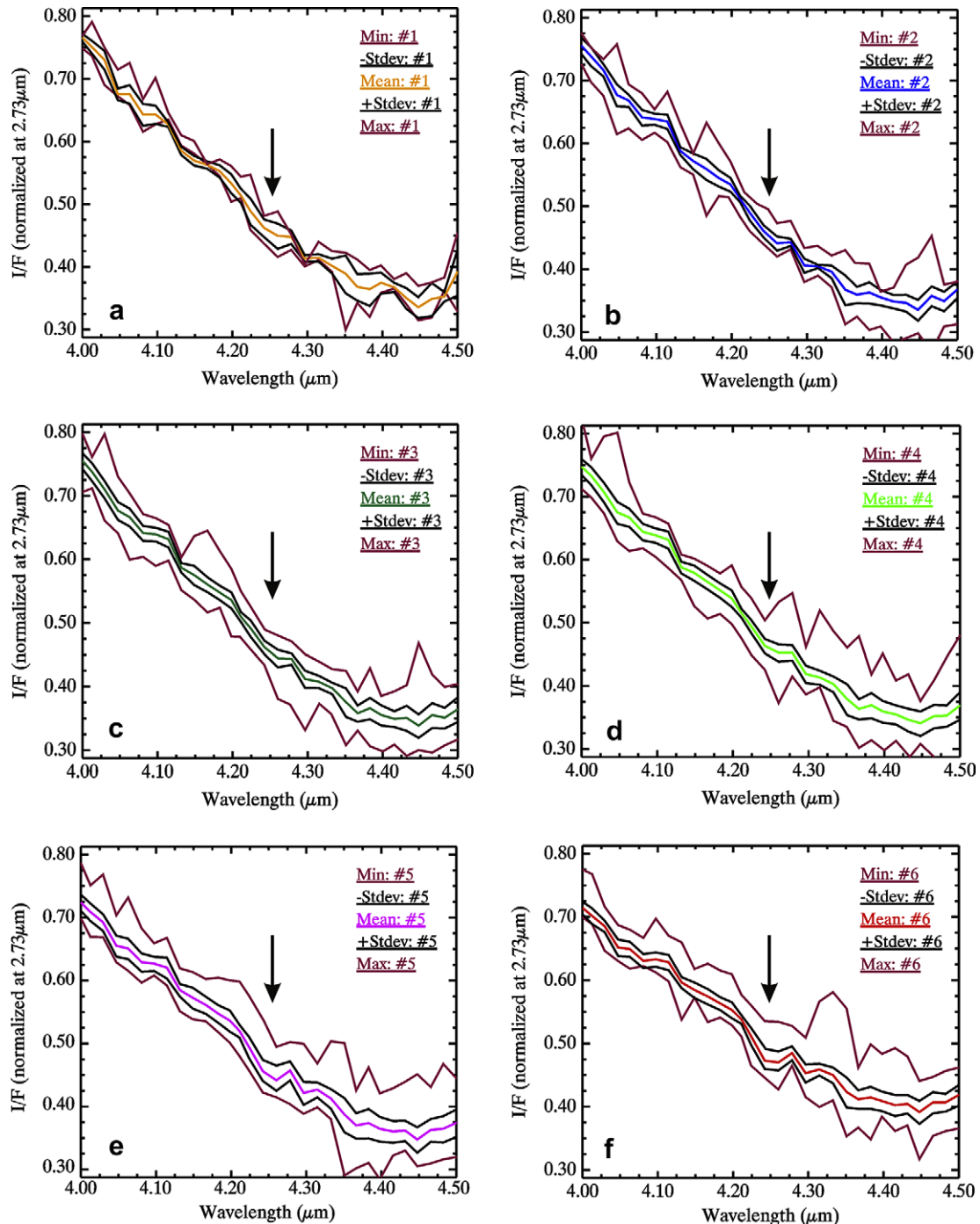
Fig. 9. Statistics (i.e. Min, −Stdev, Mean,+Stdev, Max) of the spectral classes #1 to #6 derived by SAM as in Fig. 8 separately for the wavelength range from 4 to 4.5 μm including the CO_2-absorption at 4.25 μm. The wavelength position of the CO_2-absorption is indicated by a black arrow.

analyses showed that crystalline ice does not survive very long on the surface of icy planetary objects due to space weathering processes (Hansen and McCord, 2004; Jaumann et al., 2008) that destroy the crystalline ice structure (amorphization), the combination of pure and crystalline ice characteristics could indicate fresh H_2O–ice that could point to ongoing surface processes. Little work has been done so far to simulate amorphization of H_2O–ice by irradiation on time scales relevant to Dione. Laboratory measurements, however, show that amorphization of crystalline H_2O–ice by irradiation with energetic particles is most effective at temperatures below 80 K (Dubochet and Lepault, 1984; Kouchi and Kuroda, 1990; Baratta et al., 1991; Moore and Hudson, 1992; Hudson

and Moore, 1995; Mastrapa and Brown, 2006). Although re-crystallization of amorphous H_2O–ice is known to occur upon heating above 110 K (Baragiola, 2003) it is expected to be less dominant on Dione, where the average surface temperature is 86.7 K (Smith et al., 1981). Detailed measurements, which show how temperatures vary across Dione' surface are still necessary to confirm this assumption because measurements performed for other icy satellites like the jovian satellite Callisto indicate that the surface reaches much larger temperatures during the day in regions with a relatively high degree of contamination by dark rocky material (Moore et al., 2004). Spencer et al. (2007) measured a maximum IR temperature of ~130 K in the equatorial region of the dark
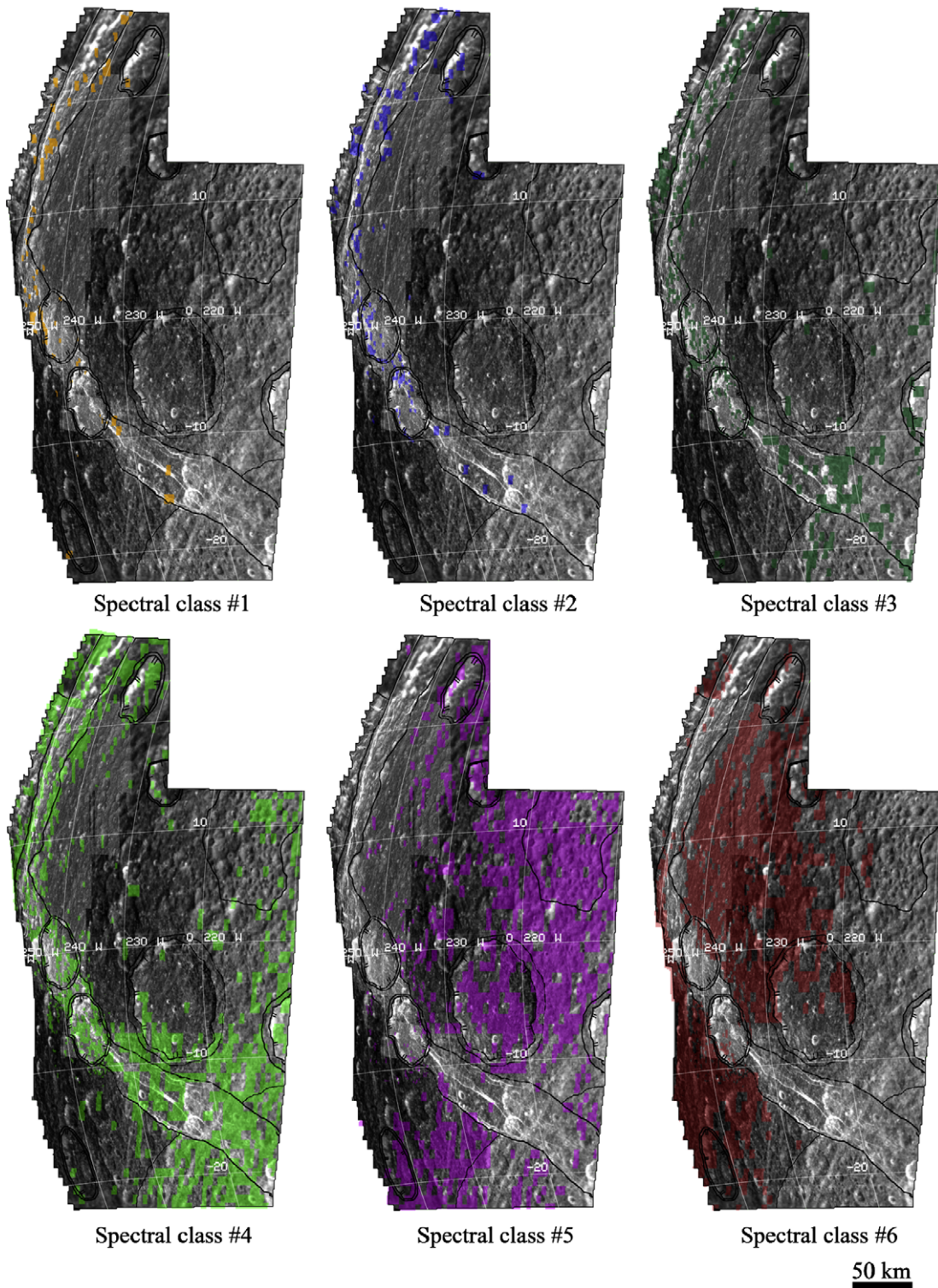
Fig. 10. Distribution of the six spectral classes derived by SAM across the Padua Chasmata region (Fig. 8) shown in a Cassini ISS mosaic with an overlay of the geological boundaries from the geological map in Fig. 4.

hemisphere of Iapetus. Since the degree of contamination of Dione's surface by dark rocky material is much less than on Iapetus a maximum surface temperature that lies distinctly below 130 K is presumed for Dione.

Fresh crystalline ice in spectral class #1 is also characterized by larger particles (Fig. 5). Similar variations could be observed on Enceladus, where smaller particles dominate the older cratered terrain and larger ones occur in the vicinity of tectonically deformed regions exhibiting material recently exposed on the surface (Jaumann et al., 2008).

The H_2O–ice signature defined in *spectral class* #1 is restricted to only 0.6% of the analyzed surface and appears as single pixels occurring especially in Aurunca and Padua Chasmata as defined in the geological map of Fig. 4 as geological units *fcp*2 and *fcp*3,
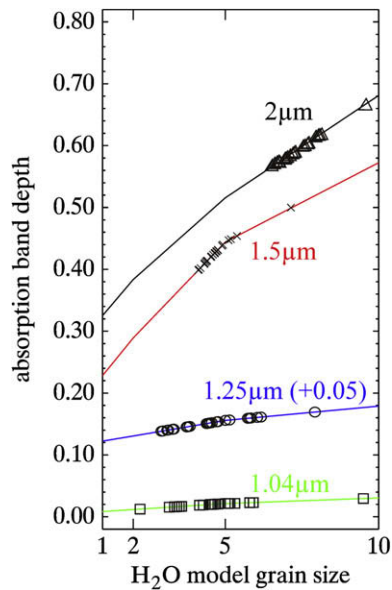
Fig. 11. Comparison of the measured depths of the H_2O-absorptions at 1.04, 1.25, 1.5 and 2 μm in the individual spectra of the spectral class #1 (indicated by symbols) to H_2O–ice models (solid lines) for specific grain radii developed by Hansen (2008).

respectively, which represent the geologically youngest units in the Padua Chasmata region.

In previous studies, two different mechanisms for the formation of the ice deposits on Dione were discussed. Smith et al. (1981) proposed that material erupted volcanically along cracks in a gas-charged system and subsequently fell back to the surface as a pyroclastic or snow-like deposit which formed the bright, linear or curved markings seen in the Voyager data termed "wispy terrain". But Cassini images and VIMS results show no evidence for such a process. In the South Polar Region (SPR) of Enceladus, icy material emanates geyser-like from the troughs, and sizes of the re-deposited ice grains decrease with increasing distance from the center of activity with respect to their specific excavation velocity (Jaumann et al., 2008). In contrast, the Padua Chasmata region contains a sharp boundary between the geological units *fcp*3 and *dcp*2 without any indication of pyroclastic material having been deposited.

Instead of cryovolcanism forming clean ice deposits, Cassini images show troughs created by tectonic stress, most likely extensional, dividing Dione's densely cratered plains (*dcp*1) into large polygons (Smith et al., 1981, 1982; Plescia, 1983; Moore, 1984), and the individual ice spots of spectral class #1 restricted to tectonic scarps represent material exposed due to extensive extensional stress causing vertical tectonic movements. Additionally, ice spots of spectral class #1 could be correlated to walls of impact craters of erosion class *c*1 that are located within or at least close to the geological units *fcp*2 and *fcp*3. The degraded morphology of these impact craters (erosion class *c*1) reveals their old age. Clean H_2O–ice is not consistent with this great age but may indicate crater walls produced by tectonic activity. Clark et al. (2008a,b) argued that pure ice is abundant on steep slopes, such as on the walls of graben facing eastward, presumably due to fresh exposure of clean ice by mass wasting on these slopes. Clean ice can be preserved on these scarps because they are protected from space weathering processes related to impacting particles from Saturn's magnetosphere that occurs on the trailing hemisphere. However, E–W-oriented slopes that belong to Aurunca Chasmata also show a clean ice spectral signature (Fig. 12b and c). These slopes appear to be morphologically quite fresh in ISS images. Since the viewing

angle is quite oblique and oriented in the E–W direction, the ISS image gives a good impression how steep these slope are, probably more than 50°. The northern part of Aurunca Chasmata representing pure H_2O–ice cuts an old impact crater wall and traverses its center (including a central peak) (Fig. 12c). Mass wasting deposits of darker material are here less pronounced than in the fracture located further to the South.

The somewhat high cratering model ages derived by Wagner et al. (2006) (Section 4) seem to contradict the bright, fresh appearance of fault scarps in unit *fcp* and the clean H_2O–ice signature. However, Wagner et al. (2006) did not distinguish between impact craters formed after the tectonic event and impact craters that were reactivated during these tectonic episodes. Further, impact craters that are younger then the tectonic events are difficult to see, if present at all, since they are situated on the steep slopes characterizing the *fcp*, which are difficult to observe directly. Therefore, the tectonic events could have continued into geologically more recent times as already suspected in Wagner et al. (2006).

Since it is not known so far how long bright ice can remain exposed without significant alteration along steep fault scarps, the exact age of the tectonic events remains an open issue. Nevertheless, the pure spectral signature of H_2O–ice implies exposed material has not yet been affected by processes such as space weathering, and therefore implies the existence of a pure water ice crust underneath the dark layer. Not much is known of Dione's internal structure so far. Usually, planetary objects characterized by a crust of pure H_2O–ice combined with a relatively high internal density ($\sim$1470 ± 12 kg m^{-3}) (Jacobson et al., 2005; http://ssd.jpl.nasa.gov) point to at least partial differentiation of the interior. Currently, in case of Dione, an ice shell with a thickness of about 240 km has been modelled when using a two layer structural model (Hussmann et al., 2006).

6.2. Spectral classes #2 (blue) and #3 (sea green)

The less icy spectral classes #2 and #3 occur mainly in the neighborhoods adjacent to the areas dominated by spectral class #1 (Fig. 10). These classes cover only a small area of the Padua Chasmata region (*spectral class* #2: 3.73%; *spectral class* #3: 5.35%) but dominate the spectral properties of the geological units *fcp*2 and *fcp*3, which themselves are spatially very limited. Note, that, although the geological units *fcp*2 and *fcp*3 are expected to be formed during different tectonic episodes (Fig. 4) no spectral differences are apparent. Either both episodes occurred in the same geological epoch, or the geologically older *fcp*2 became reactivated during the tectonic episode related to the *fcp*3.

Additionally, *spectral class* #3 occurs in association with linear, most likely tectonic features that emanate radially from a point centered at 39.8°S and 246.2°W (in older USGS maps associated with a feature named Cassandra). Although, these features are very narrow and morphologically not pronounced and therefore were not mapped as a separate geological unit (Fig. 4) they can be spectrally clearly distinguished from the geologically older units *dcp* 1 and *dcp* 2 that surround them.

6.3. Spectral class 4 (green)

As described in Sections 5 and 6, spectral class #4 contains a considerable amount of rocky non-ice material including traces of CO_2, in contrast to the icier spectral classes #1 to #3. Although, spectral class #4 covers a much larger area (21.79%) it could still be mainly associated with the geological units *fcp*2 and *fcp*3 i.e. Aurunca as well as Padua Chasmata, respectively, and often characterizes the boundary between the geological units *fcp*3 and the
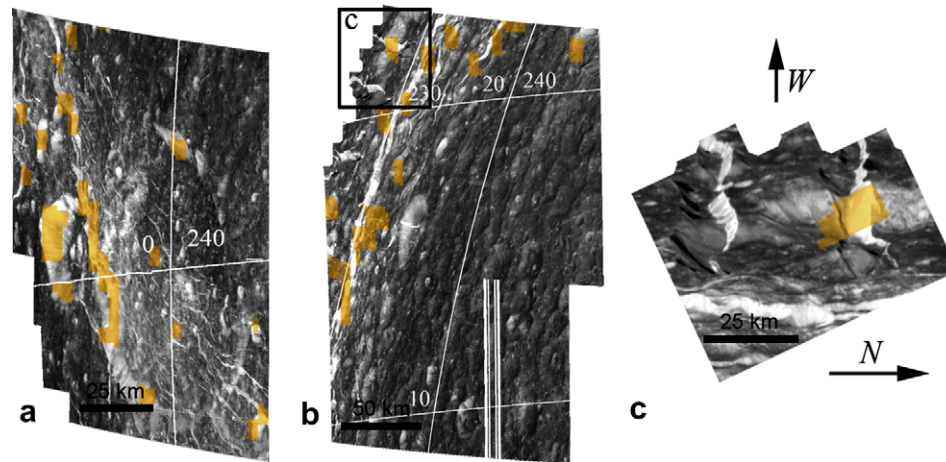
Fig. 12. Close up views of locations of pure H_2O–ice spectra of the spectral class #1 at tectonic scarps of Aurunca and Padua Chasmata as well as crater walls.

neighboring unit *dcp*2 (Fig. 10). Spectral class #4 also characterizes the linear features emanating from the Cassandra region (Fig. 4).

Moreover, this spectral class appears in parts of those impact craters located within the unit *fcp* and could be related to crater floors not affected by tectonics and, more probably, represent the spectral characteristics of the original substrate prior to tectonic events. The reason why the crater floors are spectrally still different than the old densely cratered plains (see below) can be explained by the pixel ground resolution of the VIMS observations, since the sizes of the specific regions of spectral class #4 are small compared to the corresponding VIMS pixel ground resolution of ~3 km (Fig. 11).

Spectral class #4 also characterizes the southern part of the impact crater Allecto (*c*2), the largest impact feature in the Padua Chasmata region, which is located within unit *dcp*2. Allecto lies relatively close to the tectonic regions of the Padua Chasmata (*fcp*3). Probably, tectonic processes responsible for the development of the *fcp*3 regionally influenced the neighboring regions, in this case the impact crater Allecto, as well.

Furthermore, spectral class #4 is also abundant in the most western part of our region of interest (Fig. 11), where both facies of the densely cratered plains *dcp*1 and *dcp*2 are the dominant geological units. This possibly indicates spectral behavior within the densely cratered plains independent of a specific geological unit (see below).

6.4. Spectral classes 5 (magenta) and 6 (red)

Spectral classes #5 and #6 that exhibit the highest amount of contamination with rock non-ice material and of CO_2 incorporated into the surface material cover the largest areas of the Padua Chasmata region. Spectral class #5 characterizes 31.7% and spectral class #6 still 25.4% of the investigated surface area (Fig. 10).

In general, both spectral classes are dominant in the densely cratered plains in general (i.e. both facies *dcp*1 and *dcp*2) reflecting the strongest influence of surface processes like impact cratering and space weathering. The geological unit *dcp*2 adjacent to unit *fcp*3 of the Padua Chasmata is significantly different in a spectral sense, indicated by the abrupt transition from spectral class #4 to spectral class #6 that exactly matches the boundary between these two geological units. In contrast, the transition from spectral class #5 to spectral class #6 that characterizes the western part of the *dcp*2 does not match the geological boundary between *dcp*1 and *dcp*2. This infers a distribution of the rocky non-ice material independent of Dione's geology and

may rather be related to global surface processes (see Section 7). This is also implied by the distribution of the spectral classes in the vicinity of the impact crater Allecto (−5°S/225°W), which is the most prominent geological feature within the geological unit *dcp*2 and the largest as well as the only impact crater of the erosion class *c*2 in the Padua Chasmata region (Fig. 4 and 10). Spectral class #5 covers the major part of the crater floor, whereas the spectral class #6 showing the highest degree of contamination with rocky non-ice material concentrates mainly in the western part of Allecto close to its western crater wall. This part of the crater wall is easily reached by energetic particles coming from Saturn's magnetosphere and impacting Dione from the trailing side direction as proposed by Clark et al. (2008a). Interaction between impacting particles and surface material may enhance the erosion of the uppermost surface layer eventually causing mass wasting processes resulting in the accumulation of eroded material on the crater floor (Fig. 10). In contrast, the eastern crater wall that is shielded from sputtering is characterized by the spectral class #5 like the main part of the crater floor exhibiting a slightly higher influence of H_2O ice. However, the iciest spectral class within Allecto, spectral class #4, is concentrated in the southern part of the crater floor and wall that is closest to the *fcp*3 of Padua Chasmata, implying that although regions of tectonic fractures are spatially very limited, the influence of the tectonic processes reach further into the surrounding regions and also causes the exposition of icier material characterized by spectral class #4 in this part of the crater as described above.

The responsible process for geologic unit *dcp*2 dominated by the spectral classes #5 and #6 is not clear yet. Unit *dcp*2 occurs in a number of localities, including the Padua Chasmata region (see global geologic map in Fig. 2). Both exogenic and endogenic processes may influence Dione's surface properties and could be relevant to the formation of this unit. The following formation mechanisms are possible: (1) resurfacing by degradation and deposition of material; (2) cryovolcanism; (3) impact-related processes.

Sputtering of surface ice by energetic particles from Saturn's magnetosphere, bombarding preferentially the trailing hemisphere (Clark et al., 2008a), could enhance erosion resulting in the development of a thin layer of a dark lag deposit characteristic of the *dcp* units. This lag deposit could cover small, shallow surface features including relatively small impact craters like seen in the Cassini ISS images (Fig. 3) and enhance the degradation of larger impact craters as observed locally in case of the impact crater Allecto. This process would explain the concentration of the dark rocky mate-

rial, as indicated by the spectral class #6 in the western part (closer to the center of the trailing hemisphere at 270°W) of the Padua Chasmata region and would support the implications of Clark et al. (2008a). However, such a layer would have to be several tens of meters thick in order to obliterate small craters. Therefore, an origin for unit *dcp*2 from degradation and formation of a lag deposit seems rather unlikely. The geologic unit *dcp*2 appears in the vicinity of tectonic areas of the *fcp* regions, which is also common for other occurrences of this unit. Cryovolcanism could have caused the obliteration of small craters. However, the morphology of *dcp*2 as well as digital elevation models derived with ISS data (Schenk and Moore, 2007) infer an undulating or hilly surface rather than a smooth plain indicative of a cryovolcanic resurfacing. The most likely explanation for the origin of the geological unit *dcp*2 is by impact processes. The geologic boundary to the densely cratered plains *dcp*1 more or less reflects rims and ejecta of closely spaced large craters, and the lower superimposed crater frequency in *dcp*2 suggests that these larger craters, or groups of craters, formed significantly later than unit *dcp*1. Further, the topographic measurements presented by Schenk and Moore (2007) show that old, heavily degraded impact structures occur on Dione's surface. They also identified an old impact basin as the center of the trailing side tectonics (Schenk and Moore, 2007), pointing to a relation between old impact basins and endogenic processes and possibly responsible for the resurfacing of surrounding regions. If impact processes are responsible for the *dcp*2 unit this would argue against a relation between the observed spectral properties and the emplacement of the two geological subunits *dcp*. Either spectral differences do not occur or are masked by global spectral differences (see Section 7).

In summary, relationships between, both, the spectral variations and the geological units as well as some indication that point to global effects rather than to local geology could be identified in the Padua Chasmata region. Whereas the ice-dominated spectral classes #1 to #3 characterize both facies of the *fractured cratered plains* (*fcp*2 and *fcp*3) including the bright linear features originating from the Cassandra region, the spectral classes #5 and #6 which exhibit the highest amount of rocky non-ice material as well as the minor compounds CO_2 occur exclusively in the densely cratered plains (*dcp*1 and *dcp*2).

Fresh ice spots defined by spectral class #1 exhibit relatively large ice grains and indicate fresh surface material that may be excavated due to tectonic events that could have continued into more recent times. The different tectonic events probably occurred at a comparably short time scale because no spectral differences could be identified between *fcp*2 and *fcp*3.

Despite the described spectral variations of Allecto that are related to morphological aspects no unique spectral characteristics of impact craters were observed. The analyzed craters more or less reflect the spectral properties of their substrate. Crater walls characterized by the icy spectral classes 1# to #3 are exclusively associated with impact craters located within the geological unit *fcp*2 and *fcp*3 and were interpreted as reactivated due to tectonic movements.

The "anti"-correlation of CO_2 and H_2O–ice could point to a relation of the CO_2 to the dark UV-absorber in Dione's surface material. Although the spectral classes # 5 and #6 dominate the geologically older units *dcp*1 and *dcp*2 especially the geological unit *dcp*1 shows spectral variations independent of geology which will be discussed in the following section.

7. Putting the results into regional and global context

Fig. 13 shows the *SAM* classification results using the *spectral endmembers* and classification parameters (like a maximum angle of 0.05 radians) defined for the Padua Chasmata region applied onto the whole VIMS data set of Dione. Several areas could not be classified because of saturation of the VIMS signal between ~1 and ~1.4 μm. However, using the depth of the H_2O-absorption at 2 μm a complete global spectral view of Dione's surface could be used for comparison (Fig. 14).

7.1. The Padua Chasmata region as part of Dione's trailing hemisphere

The Padua Chasmata region is part of Dione's trailing hemisphere (180–360°W). Both the classification result as well as the band depth of the H_2O–ice absorption at 2 μm indicates that the rocky non-ice material dominates Dione's trailing hemisphere expressed by the spatial distribution of the spectral class #6 and a relatively weak depth of the absorption at 2 μm and by the spatial distribution of (Figs. 13 and 14). This corresponds to an exogenic origin of the dark material caused by charged particle bombardment, as described by Clark et al. (2008a,b).

Although spectral class #6 appears exclusively in the part of the Padua Chasmata region where the geological unit *dcp*2 is dominant, this class could not be found in areas where the *dcp*2 unit is associated with impact craters (Figs. 2 and 13). In some parts, the spatial extent of the geological unit *dcp*2 is difficult to define and could not be mapped at all due to low spatial resolution and disadvantageous viewing angle of the ISS images. However, smaller areas showing surface characterization similar to the *dcp*2 unit can be identified on the Saturn-facing hemisphere that are related to impact craters and so favor an at least partial association of the whole geological unit to this geological process.

As observed in the Padua Chasmata region the remaining tectonically resurfaced areas on Dione's trailing side are dominated by the spectral classes #1, #2 as well as #3, and despite their different stratigraphic position no distinct differences in the spectral characteristics between these three geological units *fcp*1, *fcp*2 and *fcp*3 could be observed (Fig. 14). Like presumed before, either the tectonic events took place within a comparably short period of time or the older ones became reactivated during the younger tectonic episodes leading to the formation of the geological unit *fcp*3.

7.2. Transition from trailing to leading hemisphere on the anti-saturnian hemisphere

Although the anti-saturnian hemisphere (90–270°W) is mainly dominated by both facies of the geological unit *dcp* (Fig. 2), variations in the spectral characteristics independent of the geology are apparent. The whole hemisphere is dominated by the transition from less icy material on the trailing side (spectral class #6) to icier material on the leading side (spectral class #1) (Fig. 14). Despite this remarkable leading-trailing side effect no major spectral differences appear that are related to specific geologic units and/or surface features like the large impact basin *Evander* (*evb*) located at 60°S and 150°W or other geological units like the *smooth plains* (*sp*) centering near 90°W (Fig. 2) defined by Plescia (1983) and Kirchoff and Schenk (2008).

Although the spatial resolution of the global VIMS observations is relatively low (>20 km/pixel) (Table 2) compared to the highly resolved VIMS data of the Padua Chasmata region, the leading hemisphere is dominated by spectral class #1 indicating that the spectral properties of the geological unit *dcp* covering the central part of the leading hemisphere (~90°W) are similar to the tectonically resurfaced region (units *fcp*1–3) of Dione's trailing hemisphere and are characterized by clean H_2O ice.

The leading hemisphere (which is not exposed to charged particle bombardment such as observed on the trailing hemisphere) is expected to show either evidence of icy material exposed due to micro-meteoritic bombardment, as assumed for a synchro-
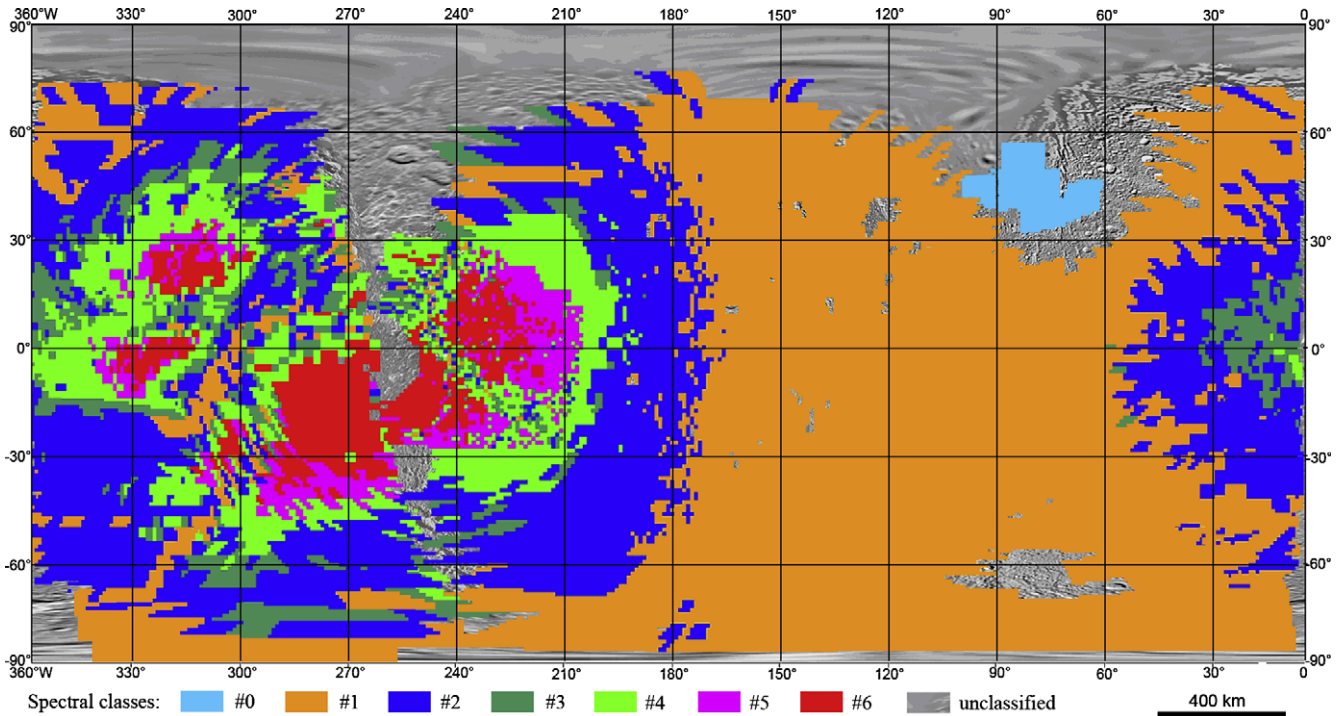
Fig. 13. SAM classification result showing the spatial distribution of the six spectral classes presented in Fig. 8 across Dione's surface, based on the local and global observations of Dione summarized in Tables 1 and 2. An additional class (spectral class #0) was needed to describe the spectral characteristics of the impact crater Creusa (~49°N/76°W) in the northern leading hemisphere.
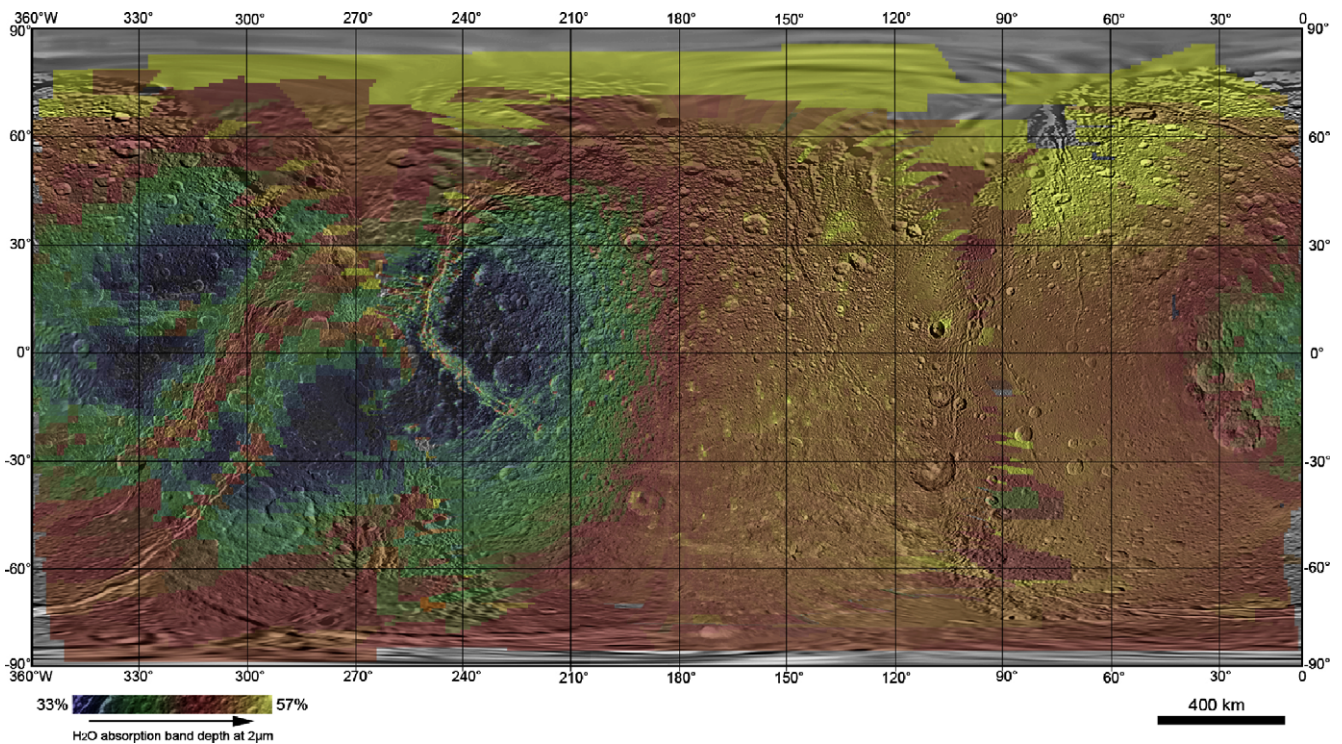

Fig. 14. Global band depth variations of the H_2O–ice absorption at 2 μm across Dione's surface as derived from local and global VIMS observations listed in Tables 1 and 2.

nously rotating satellite, or exhibits spectral characteristics of the surface material that could be related to incoming material from the E Ring coating the surface here (Buratti et al., 1990).

Sputtering effects on a synchronously rotating satellite should result in albedo differences showing a sinusoidal distribution with maximum brightness at 120 ± 30°W and minimum brightness at 290 ± 30°W (Franz and Millis, 1975; McCord et al., 1971; Blair and Owen, 1974; Noland et al., 1974; Cruikshank, 1979). Figs. 15 and 16 summarize the band depth variations at 2 μm, depending on longitude or latitude, respectively. A sinusoidal brightness func-

tion very well fits the leading-trailing transition on the anti-saturnian hemisphere especially in the equatorial region (Fig. 16). The maximum band depth occurs at 130°W fitting well to the measurements of (Cruikshank, 1979). Towards higher latitudes the longitude of maximum band depths stays constant. Only the amplitude of the sine function i.e. the range of minimum to maximum brightness decreases with increasing latitudes. Where the minimum should occur, the influence of the icy material in the geological unit *fcp* becomes obvious, expressed by the increasing band depth between 240° and 330°W. This corresponds to the region where an old, large and degraded basin detected by Schenk

and Moore (2007) is situated. On the anti-saturnian hemisphere this effect reaches an equilibrium with resurfacing effects dominating the leading hemisphere (see below) at 180°W (Fig. 16). Here the band depth at 2 μm appears to be constant from the north pole to the south pole, whereas on the trailing hemisphere equatorial regions show the strongest influence of dark material compared to the polar regions. However, if in fact the leading hemisphere of Dione should be affected by particles from the E Ring or micro-meteoritic bombardment (Buratti et al., 1990), a similar difference but opposite to the one seen on the trailing hemisphere should be detectable around 90°W. E-ring particles should impact
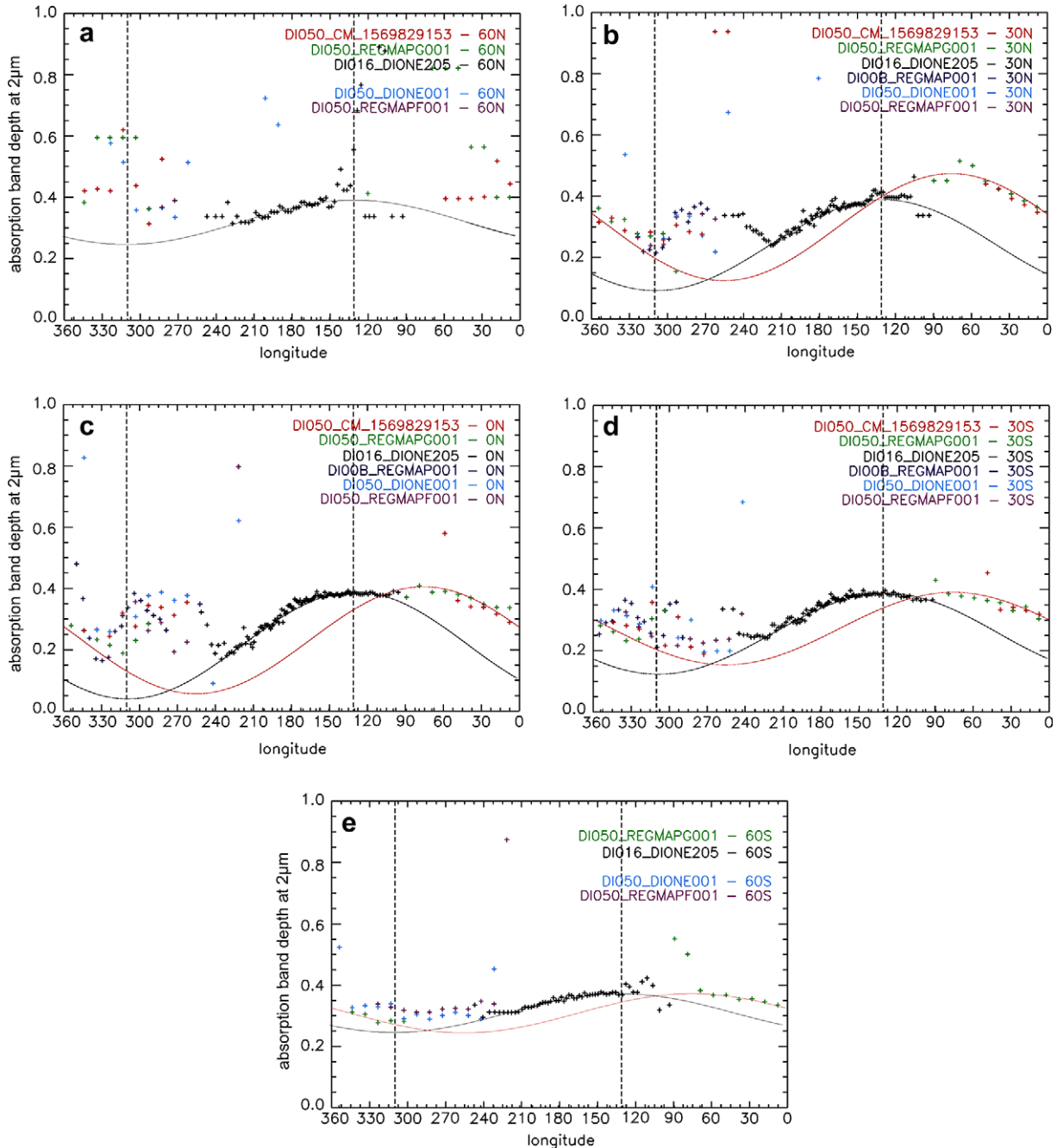

Fig. 15. Global band depth measurement profiles of the H_2O–ice absorption at 2 μm depending on longitude separately for specific latitudes i.e. (a) 60°N, (b) 30°N, (c) 0°N, (d) 30°S, (e) 60°S. A sinusoid (black curve) fitted to the data points of the anti-saturnian hemisphere (between 90°W and 270°W) represents the variations expected if the bombardment by charged particles would be the only global process influencing the spectral signal of a synchronously rotating satellite. But a second sinusoid (red curve) with a maximum at 75°W is necessary to describe the increasing of band depth at 2 μm towards the leading side of Dione. (For interpretation of the references to color in this figure legend, the reader is referred to the web version of this article.)

primarily near the equator, increasing the H_2O–ice abundance or causing at least grain size variations there. However, profiles presented in Fig. 16 show no hint of such a process.

7.3. Does a similar transition occur on the Saturn-facing hemisphere?

Despite the fact that sputtering processes from the trailing side direction cause the distribution of dark material, the sine curve describing the band depth variations of the ice absorption at 2 μm (i.e. the varying spectral influence of dark material) should fit all around Dione's surface (Fig. 16). Also the transition from the trailing hemisphere dominated by dark material to the icy leading hemisphere on the Saturn-facing hemisphere should be describable by a since curve as well. However, distinct differences between the sine curve and the actual band depth measurements

are obvious between 110° and 300°W (excluding the tectonically dominated regions between ~220° and ~330° W), caused by an enhanced spectral influence of H_2O ice, specifically by a deeper absorption at 2 μm. A second sine curve with different phase is needed; the result not only describes this transition, but also fits the band depth variations at 2 μm on the leading hemisphere, indicating a second global process affecting the spectral properties of Dione's surface material. This could be related to the proposed exogenic modification of surfaces of the Saturnian satellites by impact of micrometeoroids that 'freshens' their leading hemispheres by exposing clean ice (Smith et al., 1981; Plescia, 1983; Plescia and Boyce, 1982; Moore, 1984), or by re-deposited material coming from Enceladus and/or Saturn's E Ring.

The maximum band depth occurs in the profile near 30°N and between 60° and 90°W (Fig. 16 e). Surprisingly, this is close to
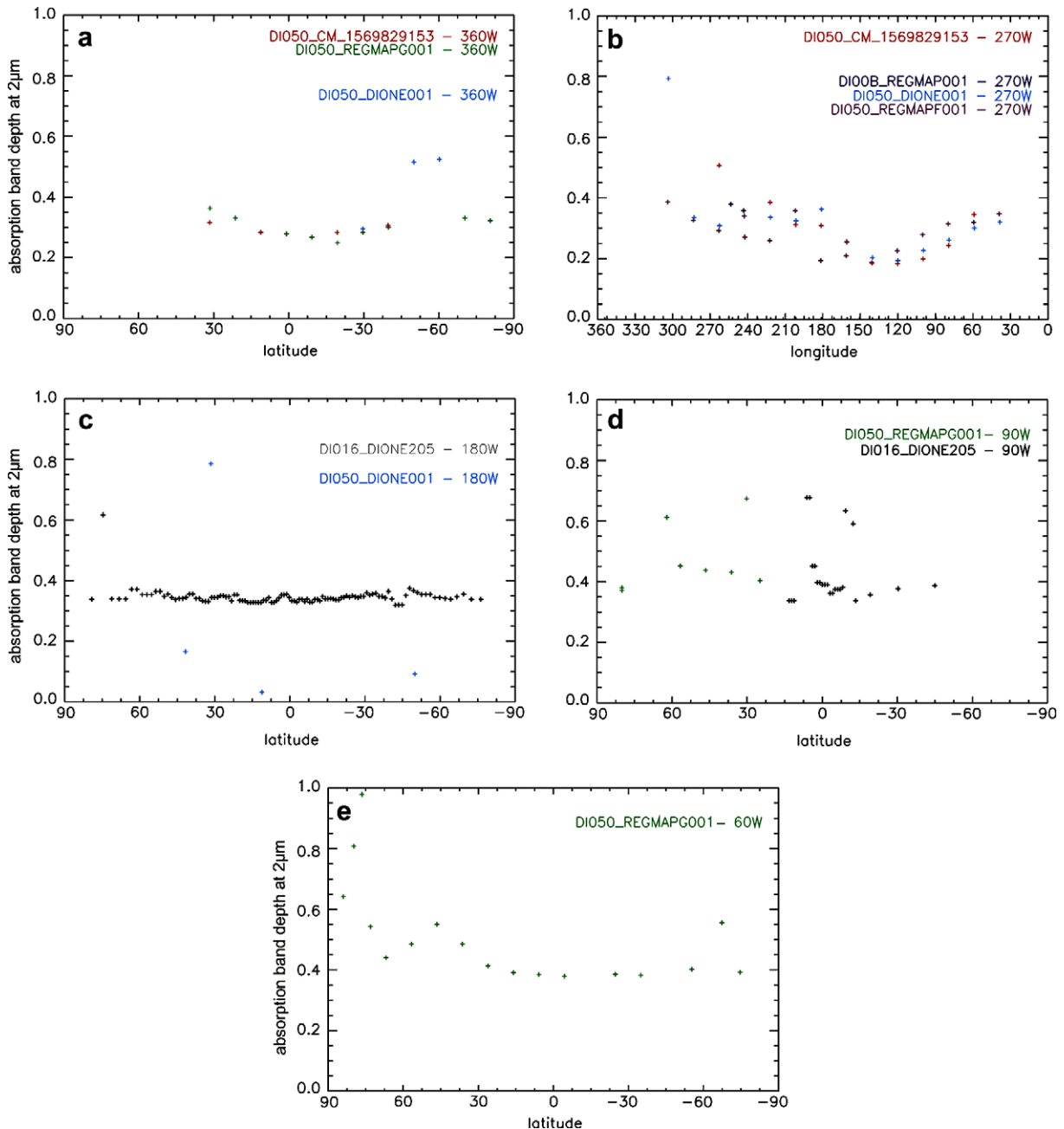

Fig. 16. Global band depth measurement profiles of the H_2O–ice absorption at 2 μm depending on latitude shown here for specific longitude (a) 360°W, (b) 270°W, (c) 180°W, (d) 90°W and (e) 60°W.
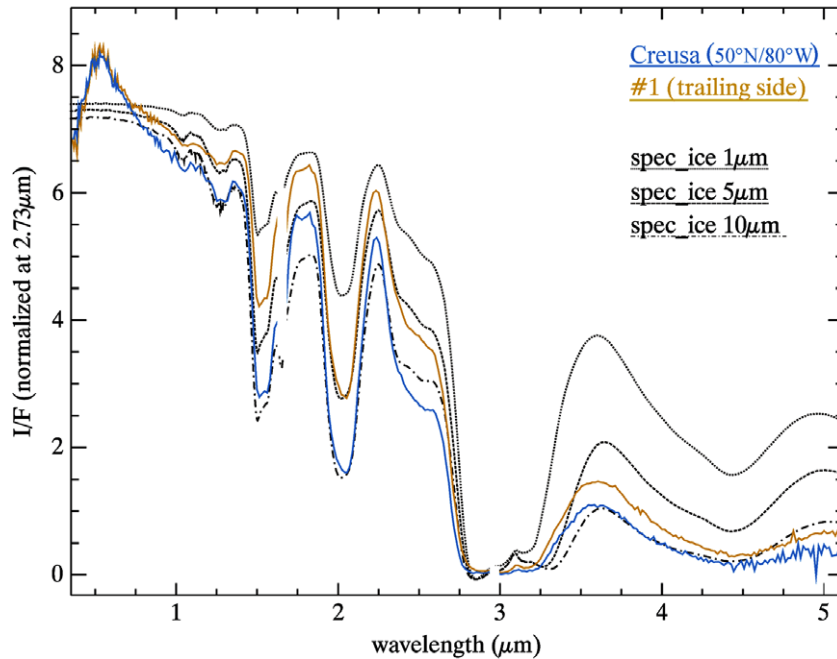
Fig. 17. Comparison of the VIMS spectrum of the impact crater Creusa (~49°N/76°W) to the spectrum of the spectral class #1 as well as H$_2$O–ice model spectra for grain radii of 1, 5, and 10 μm.

the location of the relatively young impact crater named Creusa in the northern latitudes of the leading hemisphere (~49°N/76°W) pointing to a relationship between the icier leading hemisphere of Dione and the impact process rather than exogenic modification of the surface of Dione's leading hemisphere by micrometeoroids or material from Enceladus or the E Ring.

The area corresponding to the spatial extent of Creusa and its ejecta could not be classified by *SAM*. Usually, saturation effects of the VIMS signal prohibited the classification by SAM. Looking at the spectrum of Creusa manually, however, no saturation effects were found but rather spectral characteristics that differ from the spectral classes defined in the Padua Chasmata region. The global spatial distribution of the absorption band depth at 2 μm in Fig. 14 shows a distinctly deeper H$_2$O–ice absorption associated with the impact crater itself and also its extended rays. This is supported by the comparison of the VIMS spectrum of Creusa to the ice spectrum of spectral class #1 (Fig. 17). Creusa was observed by VIMS only once during orbit 43 (April 2007). Despite the low pixel ground resolution of the VIMS observation (>30 km/pixel) the spectrum of Creusa shows not only deeper H$_2$O-absorptions but also a steeper slope from the visible towards longer wavelengths i.e. up to ~3 μm than observed in the spectral class #1, which is characteristic for larger H$_2$O-grains. Probably, variations in this spectral slope between the *endmember spectrum* of the spectral class #1 and the spectrum of Creusa locally exceed the threshold value of a maximum angle 0.05 radians used during the classification process for the definition of each spectral class and therefore can no longer be associated with the spectral class #1 anymore. Consequently a seventh spectral class (#0) was defined representing the spectral characteristics of Creusa (Fig. 17) and SAM was re-run for this new spectral class (Fig. 13). In fact the H$_2$O-particles associated with Creusa are the largest ones found on Dione' surface so far. The depths of the major H$_2$O-absorptions at 1.04, 1.25, 1.5 and 2 μm measured in the vicinity of Creusa reach up to 0.032 ± 0.04, 0.13 ± 0.035, 0.575 ± 0.028 and 0.705 ± 0.01, respectively. Whereas the SNR of the two weaker absorptions at shorter wavelength is very low relative to the band depth, and so are difficult to interpret, the measured depths of the stronger absorptions at 1.5 μm and 2 μm exceed even the values of

spectral class #1 as presented in Fig. 11 indicating grain radii of at least 10 μm.

According to the profiles in Fig. 16, the influence of Creusa reaches to a latitude of at least 30°S. Its longitudinal extension ranges westward to a longitude of at least 330°W, masking here the transition from bright to dark material as observed on the anti-saturnian hemisphere. In the eastern direction the influence of Creusa is noticeable up to 90°W without any apparent influence on the transition of the bright to dark material within the *dcp* that dominates from 110° at least up to 215°W. Here the spectral properties are likely dominated by the bombardment with energetic particles from Saturn's magnetosphere instead.

Rays of Creusa are not immediately obvious in ISS images. They become recognizable when spectral differences are enhanced by using the RGB (red/green/blue) to HIS (hue/saturation/intensity) color transformation and image ratios of the individual color filters, as described in detail by, e.g., Gillespie et al. (1986, 1987) (Fig. 18). Although the low spatial resolution of the available image data prevents the determination of an absolute crater model age of Creusa, its well preserved morphology, as well as the existence of rays, indicates a very young age less than a few tens to a few hundred million years, depending of the cratering model (Neukum et al., 2005, 2006; Zahnle et al., 2003). By coincidence, Creusa's rays seem to coalesce with tectonic scarps that cross the whole hemisphere probably influencing the spectral properties of the Saturn-facing hemisphere as well. Similar bright linear features can be observed on the anti-saturnian facing hemisphere exhibiting fresher H$_2$O ice and being depleted in CO$_2$ (spectral class #3). They, however, represent radial tectonic scarps originating from a point near the small crater named Cassandra (Wagner et al., 2005, 2006) that extend into the Padua Chasmata region and as discussed in detail above.

If there is indeed enhanced gardening by micro-meteoritic impacts or re-deposition of volcanic icy material from Enceladus or the E Ring, effects of these processes are not recognizable in the spectral data so far, possibly masked by the strong spectral signal of Creusa. Next to the signal of Creusa, only the distribution of
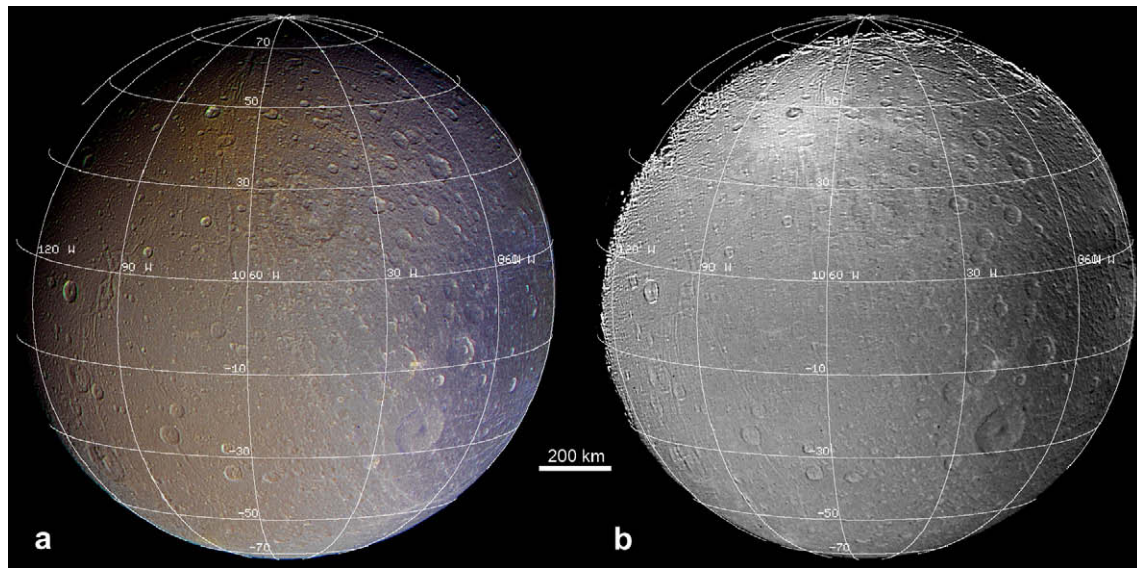
Fig. 18. Ray crater Creusa (~49°N/76°W) on Dione. (a) False color mosaic of Dione, obtained with Cassini ISS-NAC imaging data during flyby/orbit 050DI, sequence GLOCOL001. The following images taken through infrared, green, ultraviolet and clear filters (filter combination) were used for the color composite: N1569854063 (filter combination IR4/IR3), N1569853598 (CL1/GRN), N1569853513 (UV2/UV3), and N1569853291 (CL1/CL2) (see Porco et al., 2004, for a detailed description of the ISS filters). Orthographic projection centered at 9°N, 52°W, 1.2 km/pixel scale. (b) IR/UV ratio image (ISS frames N1569854063 and N1569853513) enhancing the bright ray system of crater Creusa with the same projection and scale as in (a).

the dark rocky non-ice material appears as a global process affecting the spectral properties on Dione.

7.4. What is the meaning of the global distribution of CO_2?

As noted earlier, the mapping of the CO_2-absorption at 4.25 μm across Dione's surface is difficult on a pixel by pixel basis because global observations exhibit only spatial pixel ground resolutions of 10–80 km/pixel and are often dominated by instrument-dependent noise in the wavelength region longer than 3 μm due to low signal. As done with the VIMS observations of the Padua Chasmata region (see above), eigenvectors and average spectra of the global observations listed in Table 2 were used to identify and search for variations regarding the CO_2-absorption (Fig. 19). The CO_2-absorption is distinct on the trailing hemisphere at 240°W and can still be tentatively

identified between 360° and 180°W. In the spectra of the center of the trailing hemisphere (270°W) the absorption appears slightly weaker than at 240°W. But comparison with the absorption band depth map of Fig. 14 shows that tectonic features influence the signal here. Little or no CO_2 at all was found associated with the geological unit *fcp* at a local scale implying that no CO_2 occurs in the icy crust as well as on the surface of the leading hemisphere. In contrast, on the leading hemisphere no absorption can be recognized at all. Either there is no CO_2 in the surface material on the leading hemisphere or the original surface is covered by and its spectral properties masked by other material, such as Creusa's ejecta deposits. But, including the results of our local analysis, CO_2 seems to be related to the interaction with incoming energetic particles from Saturn's magnetosphere and the emplacement or the formation of the rocky non-ice material. While the CO_2 is not in the H_2O–ice, it does not
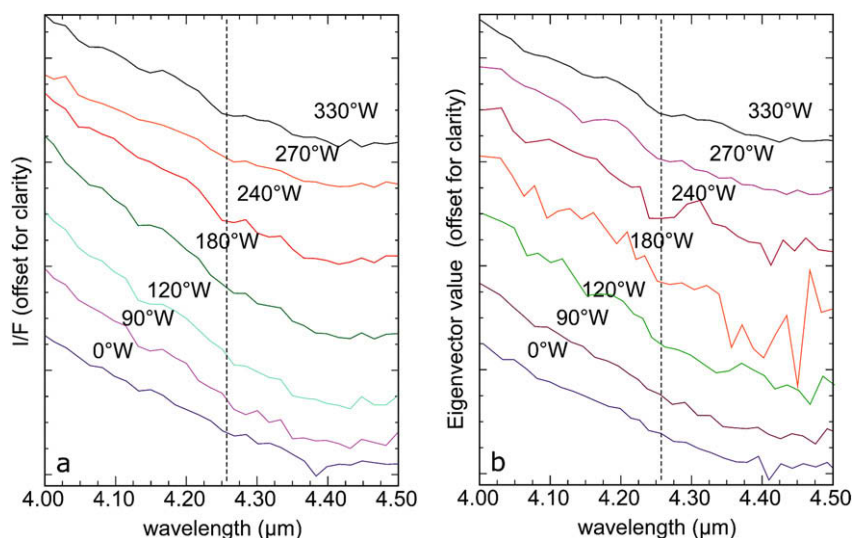

Fig. 19. Average spectra and first eigenvectors of global VIMS observations listed in Table 2 for the wavelength region between 4.0 and 4.5 μm including the CO_2-absorption at 4.26 μm (wavelength position indicated by the dashed line).

necessarily mean the CO_2 observed on Dione is not of endogenic origin. The evidence that magnetospheric processes contribute to the development of a lag deposit dominated by dark material is strong, but it is distinct from the premise that magnetospheric processes are also responsible for the CO_2 in that lag deposit. The CO_2 could pre-exist in the dark material. Although, the ice that is seen is very fine-grained (particle radii < 10 μm) exhibiting sufficient signal around 4 μm to allow the detection of a CO_2-absorption, CO_2-rich ice presumably would be less stable than pure H_2O–ice and could have sublimed. Alternatively, the formation of CO_2 in a tholin that is irradiated by Oxygen, known to be a constituent of Saturn's magnetosphere (Richardson, 1998; Richardson and Jurac, 2004; Jurac and Richardson, 2005) is intriguing.

8. Conclusions

Close views of Dione's surface properties, as well as a detailed view of its global variations, support the fact that Dione is one of the saturnian satellites with a complex history that still maintains some of its mysteries. The distribution of *spectral endmembers* as well as global band depth variations of Dione's H_2O–ice absorptions imply that the bombardment by charged particles from Saturn's magnetosphere is a major global process affecting Dione's surface. This process is responsible for the concentration of dark, non-ice material on Dione's trailing hemisphere independent of geological units (at least at a global scale), confirming the results of Clark et al. (2008a). In contrast, icy material dominates Dione's leading hemisphere. This side of Dione was thought to be mainly influenced by exogenic surface modification due to micro-meteoritic gardening that exposed clean ice (Smith et al., 1981; Plescia and Boyce, 1982; Plescia, 1983; Moore, 1984). Alternatively, it has been more recently assumed that Saturn's E Ring material was being deposited on the leading hemisphere. VIMS measurements reveal no evidence of these processes. Instead, ice deposits dominating Dione's leading hemisphere appear to be associated with rays from the fresh impact crater Creusa on the northern leading hemisphere, and with bright, linear features which seem to be an extension of the Creusa rays but more likely were created by tectonism, as the radial lineaments extending from a point near the crater Cassandra. These crater rays and bright tectonic lineaments cross almost the whole hemisphere, masking any effects of possibly existent but less dominant processes, as evident in the transition from the bright to dark regions on the Saturn-facing hemisphere (∼0°W).

No polar caps characterized by spectral properties could be identified, and the icy surface material dominating the leading hemisphere is spectrally similar to the material of the fractured cratered plains, including the depletion of minor compounds such as CO_2. In contrast, CO_2 is evident where the dark non-ice material is concentrated.

Locally, regions characterized by the strongest influence of the dark material are consistent with the emplacement of the *dcp*2, defined here as a subunit of the densely cratered plains. However, a common origin of the subunits *dcp*1 and *dcp*2 seems questionable. The most likely explanation for the origin of *dcp*2 are impacts of larger projectiles after most of unit *dcp*1 had formed, resulting in a lower superimposed frequency of smaller craters.

Several spots of pure H_2O–ice in the fractured cratered plains are indicators that tectonic processes that have continued into recent times, supporting the results of Wagner et al. (2006). VIMS data show no evidence of recent (and/or past) cryovolcanic activity that could be related to the plasma flow described by Burch et al. (2007). However, the coverage of Dione's surface beyond the Padua Chasmata region with VIMS observations exhibiting sufficient spatial resolution is still quite poor and could prevent the detection of ongoing activity in any other regions (esp. the poles) on Dione.

Despite the pronounced spectral differences of the *fcp* in comparison to the remaining geological units, as well as to fresh impact deposits, no significant differences could be observed that are related to the geology. Impact craters that are geologically relatively old mostly show spectral properties similar to their surroundings. Local spectral differences are consistent with impacting particles from the trailing side, as described by Clark et al. (2008a), with a pronounced ice signature on crater walls facing the leading side direction, which is shielded from impacting particles, and dark non-ice material concentrated on interior crater walls facing the trailing hemisphere.

The combination of both VIMS and ISS data enables the identification of pronounced differences not seen in VIMS and/or ISS images alone. The combination of high-resolution VIMS observations with sufficient signal in the wavelength region from 3 to 5 μm and of ISS camera data would potentially make it possible to map the distributions of minor surface compounds and could still greatly improve our knowledge about the compositions of the surface and of the processes responsible for their formation.

References

Baragiola, R.A., 2003. Water ice on outer solar system surfaces: Basic properties and radiation effects, Planet. Sp. Sci. 51, 953–961.

Baratta, G., Leto, G., Spinella, F., Strazzulla, G., Foti, G., 1991. The 3.1 micron feature in ion-irradiated water ice. Astron. Astrophys. 252, 421–424.

Blair, G.N., Owen, F.N., 1974. The UBV orbital phase curves of Rhea, Dione, and Tethys. Icarus 22, 224–229.

Brown, R.H., and 21 colleagues, 2004. The Cassini visual and infrared mapping spectrometer investigation. Space Sci. Rev. 115, 111–168.

Brown, R.H., and 24 colleagues, 2006. Composition and physical properties of Enceladus' surface. Science 311, 1425–1428.

Buratti, B.J., Mosher, J.A., Johnson, T.V., 1990. Albedo and color maps of the saturnian satellites. Icarus 87, 339–357.

Buratti, B.J., and 28 colleagues, 2005. Cassini visual and infrared mapping spectrometer observations of Iapetus: Detection of CO_2. Astrophys. J. 622, L149–L152.

Burch, J.L., Goldstein, J., Lewis, W.S., Young, D.T., Coates, A.J., Dougherty, M.K., André, N., 2007. Tethys and Dione as sources of outward-flowing plasma in Saturn's magnetosphere. Nature 447, 833–835. doi:10.1038/nature05906.

Clark, R.N., Roush, T.L., 1982. Reflectance spectroscopy – Quantitative analysis techniques for remote sensing application. J. Geophys. Res. 89, 6329–6340.

Clark, R.N., Brown, R.H., Owensby, P.D., Steele, A., 1984. Saturn's satellites: Near-infrared spectrophotometry (0. 65–2.5 μm) of the leading and trailing sides and compositional implications. Icarus 58, 265–281.

Clark, R.N., Fanale, F.P., Gaffey, M.J., 1986. Surface composition of natural satellites. In: Burns, J.A., Matthews, M.S. (Eds.), Satellites. Univ. of Arizona Press, Tucson, pp. 437–491.

Clark, R.N., Swayze, G.A., Livo, K.E., Kokaly, R.F., Sutley, S.L., Dalton, J.B., McDougal, R.R., Gent, C.A., 2003. Imaging spectroscopy: Earth and planetary remote sensing with the USGS tetracorder and experts system. J. Geophys. Res. 108 (E12), 5131.

Clark, R.N., and 25 colleagues, 2005. Compositional maps of Saturn's moon Phoebe from imaging spectroscopy. Nature 435, 66-69.

Clark, R.N., and 12 colleagues, 2008a. Compositional mapping of Saturn's satellite Dione with Cassini VIMS and implications of dark material in the Saturn system. Icarus 193, 372–386.

Clark, R.N., and 12 colleagues, 2008b. Compositional Mapping of Saturn's Rings and Icy Satellites with Cassini VIMS. Saturn After Cassini-Huygens, London (July).

Clark, R.N., and 10 colleagues. 2009. The composition of Iapetus: Mapping results from Cassini VIMS. Icarus, Submitted for publication. .

Crosta, A.P., Sabine, C., Taranik, J.V., 1998. Hydrothermal alteration mapping at Bodie, California, using AVIRIS hyperspectral data. Remote Sens. Environ. 65, 309–319.

Cruikshank, D.P., 1979. The surfaces and interiors of Saturn's satellites. Rev. Geophys. 17 (1), 165–176.

Cruikshank, D.P., and 30 colleagues, 2007. Surface composition of Hyperion. Nature 448, 54–57. doi:10.1038/nature05948.

Cruikshank, D.P., and 12 colleagues, the VIMS Team, 2008. Hydrocarbons on Saturn's satellites Iapetus and Phoebe. Icarus 193, 334–343. doi:10.1016/j.icarus.2007.04.036.

Cruikshank, D.P., and 17 colleagues, 2009. Carbon dioxide on the satellites of Saturn: Results from the Cassini VIMS investigation and revisions to the VIMS wavelength scale, Icarus, in press , doi:10.1016/j.icarus.2009.07.012.

De Carvalho, O.A., Meneses, P.R., 2000. Spectral Correlation Mapper (SCM); An Improvement on the Spectral Angle Mapper (SAM). Summaries of the 9th JPL Airborne Earth Science Workshop, JPL Publication 00-18, 9 p.

Dozier, J., 1989. Spectral signature of alpine snow cover from the Landsat Thematic Mapper. Remote Sens. Environ. 28, 9–22. doi:10.1016/0034-4257(1089)90101-90106.

Dubochet, J., Lepault, J., 1984. Cryo-electron microscopy of vitrified water. J. Phys. (Paris) 45. C7-85–C7-94.

Fink, U., Larson, H.P., Gautier, T.N., Treffers, R.R., 1976. Infrared spectra of the satellites of Saturn: Identification of H_2O–ice on Iapetus Rhea, Dione, and Tethys. Astrophys. J. 207, L63–L67.

Franz, O.G., Millis, R.L., 1975. Photometry of Dione, Tethys, and Enceladus on UBV system. Icarus 24, 433–442.

Gillespie, A.R., Kahle, A.B., Walker, R.E., 1986. Color enhancement of highly correlated images—I. Decorrelation and HSI contrast stretches. Remote Sens. Environ. 20, 209–235.

Gillespie, A.R., Kahle, A.B., Walker, R.E., 1987. Color enhancement of highly correlated images—II. Channel ratio and 'chromaticity' transformation techniques. Remote Sens. Environ. 22, 343–365.

Girouard, G., Bannari, A., Harti, A, Desrochers, A., 2004. Validated spectral angle mapper algorithm for geological mapping: Comparative study between quickbird and landsat-tm. In: The 20th International Society for Photogrammetry and Remote Sensing Congress, Istanbul, Turkey, July 2004, pp. 599–605.

Hansen, G.B., 2008. The comparison of single-scattering albedos from Mie calculations with Hapke estimates, LPSC XXXIX, (abstract # 2104).

Hansen, G.B., McCord, T.B., 2004. Amorphous and crystalline ice on the Galilean satellites: A balance between thermal and radiolytic processes. J. Geophys. Res. 109. doi:10.1029/2003JE002149. E001012.

Hapke, B., 1981. Bidirectional reflectance spectroscopy. 1. Theory. J. Geophys. Res. 86, 3039–3054.

Hillier, J.K., Green, S.F., McBride, N., Schwanethal, J.P., Postberg, F., Srama, R., Kempf, S., Moragas-Klostermeyer, G., McDonnell, J.A.M., Grün, E., 2007. The composition of Saturn's E ring. Monthly Notices of the Royal Astronomical Society, 377 (4), 1588–1596. doi:10.1111/j.1365-2966.2007.11710.x.

Hudson, R.L., Moore, M.H., 1995. Far-IR Spectral changes accompanying proton irradiation of solids of astrochemical interest. Radiat. Phys. Chem. 45, 779–789.

Hunter, E., Power, C.H., 2002. An assessment of two classification methods for mapping thames estuary intertidal habitats using CASI data. Int. J. Remote Sens. 23 (15), 2989–3008.

Hussmann, H., Sohl, F., Spohn, T., 2006. Subsurface oceans and deep interiors of medium-sized outer planet satellites and large trans-neptunian objects. Icarus 185 (1), 258–273.

Jacobson, R.A., and 10 colleagues, 2005. The gravity field of the saturnian system and the orbits of the major saturnian satellites. BAAS 37, 729.

Jaumann, R., and 28 colleagues, 2006. High-resolution Cassini-VIMS mosaics of Titan and the icy saturnian satellites. Planet. Space Sci. 54, 1146–1155.

Jaumann, R., and 16 colleagues, 2008. Distribution of Icy particles across Enceladus' surface as derived from Cassini-VIMS measurements. Icarus 193, 407–419. doi:10.1016/j.icarus.2007.09.013.

Jurac, S., Richardson, J.D., 2005. A self-consistent model of plasma and neutrals at Saturn: Neutral cloud morphology. J. Geophys. Res 110. doi:10.1029/2004JA010635.

Keshava, N., Mustard, J.F., 2002. Spectral unmixing. IEEE Signal Proc. 19 (1), 44–57.

Kirchoff, M., and Schenk, P., 2008. Cratering records of saturnian satellites. LPSC 39 (abstract # 2234).

Kouchi, A., Kuroda, T., 1990. Amorphization of cubic ice by ultraviolet irradiation. Nature 344, 134–135.

Kruse, F.A., Lefkoff, A.B., Boardman, J.B., Heidebrecht, K.B., Shapiro, A.T., Barloon, P.J., Goetz, A.F.H., 1993. The Spectral Image Processing System (SIPS) – Interactive visualization and analysis of imaging spectrometer data. Remote Sens. Environ. 44, 145–163 (Special issue on AVIRIS, May–June).

Lillesand, T.M., Kieffer, R.W., 2002. Remote Sensing and Image Interpretation, Fourth ed. John Wiley and Sons, ISBN 9971-51-427-3.

Mastrapa, R.M.E., Brown, R.H., 2006. Ion irradiation of crystalline H_2O-ice: Effect on the 1.65-micron band. Icarus 183, 207–214.

McCord, T.B., Johnson, T.V., Elias, J.H., 1971. Saturn and its satellites: Narrow band spectrophotometry (0.3-1.1 μm). Astrophys. J. 165, 413–424.

Moore, J.M., 1984. The tectonic and volcanic history of Dione. Icarus 59, 205–220.

Moore, M.H., Hudson, R.L., 1992. Far-infrared spectral studies of phase changes in water ice induced by proton irradiation. Astrophys. J. 401, 353–360.

Moore, J.M., Schenk, P.M., Bruesch, L.S., Asphaug, E., McKinnon, W.B., 2004. Large impact features on middle-sized icy satellites. Icarus 171, 421–443.

Neukum, G., 1985. Cratering records of the satellites of Jupiter and Saturn. Adv. Space Sci. 5 (8), 107–116.

Neukum, G., Wagner, R.J., Denk, T., Porco, C.C., the Cassini ISS Team, 2005. The cratering record of the saturnian satellites Phoebe, Tethys, Dione and Iapetus in comparison: First results from analysis of the Cassini ISS imaging data. Lunar Planet. Sci. Conf. 36th (abstract 2034).

Neukum, G., Wagner, R.J., Wolf, U., Denk, T., 2006, The Cratering Record and Cratering Chronologies of the Saturnian Satellites and the Origin of Impactors: Results from Cassini ISS Data. 1st Europlanet Conference, EPSC2006-A-00610, Berlin, 22 September 2006.

Noland, M., Veverka, J., Morrison, D., Cruikshank, D.P., Lazarewicz, A.R., Morrison, N.D., Elliot, J.L., Goguen, J., Burns, J.A., 1974. Six-color photometry of Iapetus, Titan, Rhea, Dione, and Tethys. Icarus 23, 334–354.

Plescia, J.B., Boyce, J.M., 1982. Crater densities and geological histories of Rhea, Dione, Mimas and Tethys. Nature 295, 285–290.

Plescia, J.B., 1983. The geology of Dione. Icarus 56, 255–277.

Plescia, J.B., Boyce, J.M., 1985. Impact cratering history of the saturnian satellites. J. Geophys. Res. 90 (B2), 2029–2037.

Porco, C.C., and 19 colleagues, 2004. Cassini imaging science: Instrument characteristics and capabilities and anticipated scientific investigations at Saturn. Space Sci. Rev., 115, 363–497. doi:10.1007/s11214-004-1456-7.

Porco, C.C., and 24 colleagues, 2006. Cassini observes the active south pole of Enceladus. Science 311 (5766): 1393–1401. AAAS. doi:10.1126/science.1123013.

Prockter, L.M., and 14 colleagues, 1998. Dark terrain on Ganymede – Geological mapping and interpretation of Galileo Regio at high resolution. Icarus 135, 317–344.

Richards, I.A., Jia, X., 1996. Remote Sensing Digital Image Analysis – An Introduction, 3rd ed. Springer.

Richardson, J.D., 1998. Thermal plasma and neutral gas in Saturn's magnetosphere. Rev. Geophys. 36, 501–524.

Richardson, J.D., Jurac, S., 2004. A self-consistent model of plasma and neutrals at Saturn: The ion tori. Geophys. Res. Lett. 31, L24803.1–L24803.4.

Roatsch, T., Wählisch, M., Hoffmeister, A., Matz, K.D., Scholten, F., Kersten, E., Wagner, R., Denk, T., Neukum, G., Porco, C., 2008. High-resolution Dione atlas derived from Cassini-ISS images. Planet. Space Sci. 56, 1499–1505.

Schenk, P.M., Moore, J.M., 2007. Impact crater topography and morphology on saturnian mid-sized satellites. LPSC XXXVIII, 2305.

Schwarz, I., Staenz, K., 2001. Adaptive threshold for spectral matching of hyperspectral data. Can. J. Remote Sens. 27 (3), 216–224.

Shkuratov, Y., Starukhina, L., Hoffmenn, H., Arnold, G., 1999. A model of spectral albedo of particulate surfaces: Implications for optical properties of the Moon. Icarus 137, 235–246.

Seidelmann, P.K.and 10 colleagues, 2002. Report of the IAU/IAG Working Group on Cartographic Coordinates and Rotational Elements of the Planets and Satellites: 2000. Celestial Mech. Dynam. Astron. 82, 83–111.

Smith, B.A., and 26 colleagues, 1981. Encounter with Saturn: Voyager 1 imaging science results. Science 212, 163–191. doi:10.1126/science.212.4491.163.

Smith, B.A., and 28 colleagues, 1982. A new look at the Saturn system: The Voyager 2 images. Science 215, 504–536. doi:10.1126/science.215.4532.504.

Spahn, F., and 15 colleagues, 2006. Cassini dust measurements at enceladus and implications for the origin of the E ring. Science 311 (5766): 1416–1418. AAAS. doi:10.1126/science.1121375.

Spencer, J.R., Pearl, J.C., Segura, M., Cassini CIRS Team, 2007. Cassini composite infrared spectrometer (CIRS) observations of Iapetus' thermal emission, and implications for the hemispheric asymmetry. In: 39th DPS Meeting, Orlando, #P22C-04.

Stephan, K., 2006. Chemisch-physikalische Zusammensetzung der Ganymedoberfläche: Zusammenhänge mit geologischen Strukturen und deren Gestaltungsprozessen. Ph.D. thesis, Freie Universität Berlin, 249 pp., http://www.diss.fu-berlin.de/2006/343/index.html.

Stephan, K., and 13 colleagues, 2008a. Relationship of Dione's spectral properties to geological surface units. LPSC XXXIX, 1717.

Stephan, K., Hibbitts, C.A., Hoffmann, H., Jaumann, R., 2008b. Reduction of instrument-dependent noise in hyperspectral image data using the principal component analysis: Applications to Galileo NIMS data. Planet. Space Sci. 56, 406–419.

Thomas, P.C., and 12 colleagues, 2007b. Shapes of the saturnian icy satellites and their significance. Icarus 190, 573–584. doi:10.1016/j.icarus.2007.03.012.

Thekekara, M.P., 1973. Solar energy outside the Earth's atmosphere. Sol. Energy 14, 109–127.

Van der Meer, F., Vasquez-Torres, M., Van Dijk, P.M., 1997. Spectral characterization of ophiolite lithologies in the troodos ophiolite complex of cyprus and its potential in prospecting for massive sulphide deposits. Int. J. Remote Sens. 18 (6), 1245–1257.

Wagner, R.J., Neukum, G., Denk, T., and the Cassini ISS Team, 2005. Bull. Am. Astron. Soc. 37 (3), 701 (Abstr. 36-02).

Wagner, R., Neukum, G., Giese, B., Roatsch, T., Wolf, U., Denk, T., the Cassini ISS Team, 2006. Geology, ages and topography of Saturn's satellite Dione observed by the Cassini ISS camera. LPSC XXXVII, 1805, 2006.

Wagner, R.J., Neukum, G., Giese, B., Roatsch, T., Wolf, U., 2007. The global geology of Rhea: Preliminary implications from the Cassini ISS data. LPSC XXXVIII, 1958.

Wilhelms, D.E., 1990. Geologic mapping. In: Greeley, R., Batson, R.M. (Eds.), Planetary Mapping, vol. 6. Cambridge Planet. Sci. Series, Cambridge, U.K, pp. 208–260.

Yuhas, R.H., Goetz, A.F.H., Boardman, J.W., 1992. Discrimination among semi-arid landscape endmembers using the spectral angle mapper (SAM) algorithm. In: Summaries of the 4th JPL Airborne Earth Science Workshop, JPL Publication 92-41, pp. 147–149.

Zahnle, K., Schenk, P., Levison, H., Dones, L., 2003. Cratering rates in the outer Solar System. Icarus 163, 263–289.